

1 **In-situ observations of the isotopic composition of methane at the**
2 **Cabauw tall tower site**

3

4 Thomas Röckmann^{1,*}, Simon Eyer^{2,*}, Carina van der Veen¹, Maria E. Popa¹, Béla
5 Tuzson², Guillaume Monteil^{1,3}, Sander Houweling¹, Eliza Harris², Dominik
6 Brunner², Hubertus Fischer⁷, Giulia Zazzeri⁴, David Lowry⁴, Euan G. Nisbet⁴, Willi
7 A. Brand⁵, Jaroslav M. Necki⁶, Lukas Emmenegger² and Joachim Mohn²

8

9 ¹ Utrecht University (UU), Institute for Marine and Atmospheric Research
10 Utrecht (IMAU), The Netherlands

11 ² Empa, Laboratory for Air Pollution / Environmental Technology, Dübendorf,
12 Switzerland

13 ³ now at Department of Physical Geography and Ecosystem Science, Lund
14 University, Lund, Sweden

15 ⁴ Royal Holloway University of London (RHUL), Department of Earth Sciences,
16 Egham, UK

17 ⁵ Max-Planck-Institute (MPI) for Biogeochemistry, Jena, Germany

18 ⁶ Environmental Physics Group, Faculty of Physics and Applied Computer
19 Science, AGH University of Science and Technology, Krakow, Poland

20 ⁷ University of Bern, Climate and Environmental Physics, Bern, Switzerland

21

22 *These authors contributed equally to this work

23

24

25 **Abstract**

26 High precision analyses of the isotopic composition of methane in ambient air
27 can potentially be used to discriminate between different source categories. Due
28 to the complexity of isotope ratio measurements, such analyses have generally
29 been performed in the laboratory on air samples collected in the field. This poses
30 a limitation on the temporal resolution at which the isotopic composition can be
31 monitored with reasonable logistical effort. Here we present the performance of
32 a dual isotope ratio mass spectrometric system (IRMS) and a quantum cascade
33 laser absorption spectroscopy (QCLAS) based technique for in-situ analysis of
34 the isotopic composition of methane under field conditions. Both systems were
35 deployed at the Cabauw experimental site for atmospheric research (CESAR) in
36 the Netherlands and performed in-situ, high-frequency (approx. hourly)
37 measurements for a period of more than 5 months. The IRMS and QCLAS
38 instruments were in excellent agreement with a slight systematic offset of (+0.25
39 \pm 0.04) ‰ for $\delta^{13}\text{C}$ and (-4.3 \pm 0.4) ‰ for δD . This was corrected for, yielding a
40 combined dataset with more than 2500 measurements of both $\delta^{13}\text{C}$ and δD . The
41 high precision and temporal resolution dataset does not only reveal the
42 overwhelming contribution of isotopically depleted agricultural CH_4 emissions
43 from ruminants at the Cabauw site, but also allows the identification of specific
44 events with elevated contributions from more enriched sources such as natural
45 gas and landfills. The final dataset was compared to model calculations using the
46 global model TM5 and the mesoscale model FLEXPART-COSMO. The results of
47 both models agree better with the measurements when the TNO-MACC emission
48 inventory is used in the models than when the EDGAR inventory is used. This
49 suggests that high-resolution isotope measurements have the potential to
50 further constrain the methane budget, when they are performed at multiple sites
51 that are representative for the entire European domain.

52 **1. Introduction**

53 The global increase of the important greenhouse gas methane in the atmosphere
54 since the beginning of the industrial period is very well established
55 (Dlugokencky et al., 2009; Dlugokencky et al., 1996; Dlugokencky et al., 1998;
56 Etheridge et al., 1998; Khalil et al., 2007; Loulergue et al., 2008; MacFarling
57 Meure et al., 2006; Rasmussen and Khalil, 1981; Spahni et al., 2005). The existing
58 CH₄ mole fraction measurement data enable accurate assessment of the source-
59 sink imbalance through time, and together with the estimated total sink strength,
60 they allow for a top-down constraint on the global source of methane to the
61 atmosphere (Bergamaschi et al., 2013; Houweling et al., 2014). Bottom-up
62 estimates of the global methane budget carry much larger uncertainties, which
63 are inherent to the assumptions made in the extrapolation of local scale
64 measurements to larger scales (Bruhwiler et al., 2014; Kirschke et al., 2013;
65 Nisbet et al., 2014). The advantage of bottom-up estimates is, however, the
66 possibility to distinguish different sources and to link observations to process-
67 level understanding of the emissions.

68 An independent approach for distinguishing between source categories of CH₄ is
69 the analysis of its isotopic composition, which is strongly linked to the
70 source/sink processes. This is particularly true for methane from biogenic,
71 thermogenic and pyrogenic sources (Gros et al., 2004; Houweling et al., 2008;
72 Quay et al., 1999; Sapart et al., 2012). A more detailed differentiation within one
73 source category, e.g. biogenic CH₄, for emissions from wetlands, ruminants, rice
74 paddies or termites, however, is complicated because of the overlap of the
75 respective isotopic source signatures. Further complications arise because
76 individual source signatures can show pronounced dependence on
77 environmental parameters and metabolized substrates (Kawagucci et al., 2014;
78 Klevenhusen et al., 2010). In addition to the source contributions, the sink
79 processes (mainly chemical removal by the hydroxyl radical (OH), but also soil
80 deposition and stratospheric loss) also affect the isotopic composition of
81 atmospheric methane (Brenninkmeijer et al., 1995; Röckmann et al., 2011;
82 Saueressig et al., 1996; Saueressig et al., 2001; Snover and Quay, 2000).
83 Nevertheless, over the past decades, numerous studies have shown the potential
84 of isotope measurements to identify individual source categories from isotope

85 observations (Beck et al., 2012; Lassey et al., 1993; Tarasova et al., 2006;
86 Umezawa et al., 2012b; Zazzeri et al., 2015) and to constrain budgets (Ferretti et
87 al., 2005; Fischer et al., 2008; Houweling et al., 2008; Lassey et al., 2000; Lowe et
88 al., 1994; Sapart et al., 2012; Umezawa et al., 2012a).

89 The isotopic composition is commonly reported in δ notation, where δ quantifies
90 the relative deviation of an isotope ratio ($^{13}R = ^{13}\text{C}/^{12}\text{C}$ for carbon isotopes and 2R
91 $= ^2\text{H}/^1\text{H}$, abbreviated as D/H, for hydrogen isotopes) in a sample from a standard
92 ratio. The international standard for reporting $\delta(^{13}\text{C}, \text{CH}_4)$ values is Vienna Pee
93 Dee Belemnite (VPDB, $^{13}R_{\text{VPDB}} = 0.0112372$ (Craig, 1957)) and for $\delta(\text{D}, \text{CH}_4)$ it is
94 Vienna Standard Mean Ocean Water (VSMOW, $^2R_{\text{VSMOW}} = 0.0020052$ (Baertschi,
95 1976)). $\delta(^{13}\text{C}, \text{CH}_4)$ and $\delta(\text{D}, \text{CH}_4)$ are abbreviated as $\delta^{13}\text{C}$ and δD in the following,
96 and given in per mill (‰). CH_4 mole fractions $\chi(\text{CH}_4)$ are reported in nmol/mol =
97 10^{-9} and $\mu\text{mol/mol} = 10^{-6}$. For interpretation of global or continental scale
98 atmospheric data the expert group of the WMO/IAEA has set a scientifically
99 desirable level of compatibility of 2 nmol/mol, 0.02 ‰ and 1 ‰ for CH_4
100 fraction, $\delta^{13}\text{C}$ and δD , respectively (WMO, 2014). For regionally focused studies
101 with large local fluxes, extended compatibility goals of 5 nmol/mol, 0.2 ‰ and 5
102 ‰ for $\chi(\text{CH}_4)$, $\delta^{13}\text{C}$ and δD were defined.

103 Due to the complexity of the involved measurement techniques, CH_4 isotope
104 measurements have been limited mostly to relatively low frequency sampling in
105 the field followed by isotope analysis in the laboratory (Bock et al., 2010; Brass
106 and Röckmann, 2010; Sapart et al., 2011; Sperlich et al., 2013; Umezawa et al.,
107 2009; Yamada et al., 2003). For many decades, the dominant method for high
108 precision isotope analysis of atmospheric methane was isotope ratio mass
109 spectrometry. In particular, the development of continuous-flow IRMS in the past
110 two decades (Merritt et al., 1994; Merritt et al., 1995) has greatly increased the
111 throughput of IRMS methods, making this the technique of choice in most
112 laboratories, also because of the small sample amounts required.

113 Recently, mid-infrared laser absorption spectroscopy has proven its potential for
114 high precision isotope ratio analysis. First attempts of measuring the isotopic
115 composition of methane (Bergamaschi et al., 1998a; 1998b; 1994) were
116 restricted to enhanced CH_4 fractions ($>50 \mu\text{mol/mol}$ for $\delta^{13}\text{C}$ and >2000

117 $\mu\text{mol/mol}$ for δD) and required cryogenic cooling for both the laser source and
118 the detector, which impeded in-situ and long-term applications. The invention of
119 room temperature, quantum cascade laser (QCL) sources has triggered the
120 development of a novel generation of spectrometers suitable for in-situ analysis
121 of the isotopic composition of greenhouse gases (Eyer and al, 2015; Tuzson et al.,
122 2008; Wächter et al., 2008). Their capability of high-temporal resolution led to
123 new applications aiming for source attribution (Mohn et al., 2012; Tuzson et al.,
124 2011; Wolf et al., 2015). The advantages of in-situ measurements are particularly
125 apparent in combination with atmospheric modeling techniques, which enables
126 the identification of specific source regions (Rigby et al., 2012; Sturm et al.,
127 2013). Similarly, high-frequency, high-precision CH_4 isotope data are expected to
128 greatly reduce uncertainties of national and global source estimations, as
129 demonstrated in an observing system simulation experiment (Rigby et al., 2012).
130 In this paper we present the analytical setup and results of a 5-month campaign
131 at the Cabauw tall tower site in the Netherlands, where the isotopic composition
132 ($\delta^{13}\text{C}$ and δD) of CH_4 was measured with two instruments, one IRMS system
133 developed at Utrecht University and one QCLAS-instrument developed at Empa.
134 The compatibility of the two analytical techniques for CH_4 mole fractions, $\delta^{13}\text{C}$ -
135 CH_4 and δD - CH_4 is assessed and the obtained high-resolution isotope dataset is
136 exploited using a novel moving Keeling plot method. A comparison of
137 measurement results with calculations from two different models (TM5 and
138 FLEXPART-COSMO) and two emission inventories (EDGAR, TNO-MACC)
139 indicates the potential of this approach to better constrain on isotope source
140 signatures and emissions in atmospheric models.

141 **2. Methods**

142 **2.1. Site description**

143 The 213 m tall tower is the central construction of the Cabauw Experimental Site
144 for Atmospheric Research (CESAR, <http://www.cesar-observatory.nl/>, $51^\circ 58' \text{N}$,
145 $4^\circ 55' \text{E}$, 2 m a.s.l.). The CESAR site is dedicated to atmospheric research and
146 hosts a wide variety of instruments for in situ and remote sensing measurements
147 of meteorological parameters, trace gases, pollutants, aerosols, and clouds. The

148 site is located in an agricultural landscape, with CH₄ emissions originating from
149 ruminants and other agricultural activities, but also from the peaty soil and the
150 drainage ditches between the surrounding fields (Peltola et al., 2014). The small
151 town Lopik (~7500 inhabitants) is located 1 km east of the tower. Population
152 and road density increase steeply further away from the tower towards the
153 country's major cities: Utrecht (at about 20 km distance), Rotterdam (30 km), the
154 Hague (40 km) and Amsterdam (45 km). An estimated seven million people
155 inhabit these cities and their many neighboring settlements. The location and
156 surroundings are described in more detail in (Peltola et al., 2014; Peltola et al.,
157 2015; Vermeulen et al., 2011). The instruments were operated in a room on the
158 ground floor of the CESAR building. Since this room is not commonly used as
159 laboratory, it has air-conditioning with limited cooling capacity and the
160 temperature varied between 25 °C and 30 °C.

161 **2.2. Air sampling at the Cabauw tall tower**

162 Air was continuously drawn through ½ inch o.d. (outer diameter) Dekabon
163 tubing from 20 m height at a total flow of 16 l min⁻¹ (STP) provided by a Varian
164 scroll pump (Agilent Technologies Inc., USA). The sample gas flow was adjusted
165 by means of a flow restriction at the inlet of the pump in order to maintain the
166 pressure in the sampling line above 950 hPa. The sample gas flows for the
167 methane isotope analyzers were branched off upstream of the scroll pump and
168 the restriction, using ¼ inch o.d. Dekabon lines.

169 **2.3. IRMS system**

170 The new IRMS method for δ¹³C and δD analysis of atmospheric CH₄ is based on
171 the ISAAC system as developed at the MPI for Biogeochemistry in Jena (Brand et
172 al., 2016). Importantly, the system does not require liquid nitrogen coolant for
173 the preconcentration and focusing steps, but uses a massive copper block cooled
174 down to about -145 °C, to which the cold traps for preconcentration and cryo-
175 focussing are connected via standoffs (see 2.3.1). This cold assembly is contained
176 in an evacuated steel Dewar to prevent condensation of moisture. During the
177 campaign, the extraction unit and two IRMS instruments (Thermo Delta Plus XL
178 for hydrogen isotopes and Thermo Delta Plus XP for carbon isotopes, both

179 Thermo Fisher Scientific Inc., Germany) were operated at the CESAR site. The
180 system is schematically shown in Fig. 1.

181 **2.3.1. Cryogenic trapping**

182 A Polycold compact cooler compressor (Brooks Automation Inc., USA), filled with
183 coolant PT-30, cooled a cold end on which a copper cylinder (70 mm diameter,
184 85 mm height, 3 kg) was mounted. In this configuration, the copper block
185 reached a temperature of -145 °C. The pre-concentration trap (PreCon) was a 10
186 cm 1/8 inch SS tube filled with 4 cm 60/80 mesh HayeSep D in the center and 3
187 cm 60/80 glass beads on each end. It was connected with Valco fittings and the
188 packing material was retained in the trap using removable frits (CEF1F, Valco
189 Instruments Company Inc., USA). The focus trap (Focus) was a 10 cm 1/16 inch
190 SS tube filled with 2 cm HayeSep D and 4 cm glass beads at both ends, connected
191 with Valco fittings (ECEF211.0F, Valco Instruments Company Inc., USA). The
192 traps could be heated with 0.5 m Thermsys heating wire wrapped around the
193 tubes. The PreCon and Focus trapping units were glued together with a PT-100
194 temperature sensor in heat - conducting two component epoxy on a brass
195 standoff. These brass standoffs were mounted to the copper cylinder. In the
196 “trapping” configuration the temperatures of the traps were usually kept at -135
197 °C.

198 **2.3.2. Measurement procedure**

199 A 3-port 2-position Valco valve (3PV, Fig. 1) selected either ambient air drawn
200 from the tower through a $\text{Mg}(\text{ClO}_4)_2$ dryer, or cylinder air that was injected via
201 one port of an 8-port multiposition Valco valve (MPV). To check the system
202 performance, a reference air cylinder (Ref) was measured alternately with
203 ambient air, and three other target gas cylinders were measured occasionally.
204 The inlet line was connected to a 4-port 2-position Valco valve (4PV1), which
205 directed either Helium (He, BIP quality, Air Products and Chemicals Inc., USA) or
206 the selected airflow to the PreCon unit, which was connected in the loop position
207 of a 6-port 2-position Valco valve (6PV). All He and air flows were controlled by
208 MKS mass flow controllers (MFC, MKS Instruments Inc., USA).

209 The preconcentration and cryofocussing was done similarly to Brass and

210 Röckmann (2010). After flushing the inlet line with >20 ml air, the 6PV was
211 switched to the load position and air was admitted to the PreCon unit. The
212 duration of the air sampling for the IRMS system was 10 minutes at a flow rate of
213 5 ml min⁻¹ for $\delta^{13}\text{C}$ and 7 ml min⁻¹ for δD (273 K, 1 bar). The flow was provided
214 by a Xavitech mini pump (P200-GAS-12V, Xavitech AB, Sweden). During this step,
215 the temperature measured at the PreCon stayed below -132 °C. At this
216 temperature CH₄ and several other trace species were retained on the HayeSep
217 D, while the air matrix was efficiently flushed out.

218 After preconcentration, the PreCon unit was heated to -30 °C and a He flow of
219 4 ml min⁻¹ (273 K, 1 bar) transported the CH₄ in 90 seconds to the Focus unit,
220 which was held at a temperature <-137 °C. After transfer of the sample to the
221 Focus, the 6PV was switched to the load position and the PreCon was heated to -
222 10 °C to release any remaining trapped gases such as CO₂.

223 The Focus was then heated to release the CH₄, which was directed via 4PV2 and
224 4VP3 either to the combustion oven and the Delta plus XP IRMS for ¹³C analysis
225 or to the pyrolysis oven and the Delta plus XL IRMS for D analysis.

226 For δD analysis, the CH₄ was injected into a pyrolysis tube furnace (1400 °C),
227 where CH₄ was converted to H₂ and carbon. The H₂ entered the IRMS, after
228 passing a 2 m CarboPLOT column at room temperature (RT) and a nafion dryer,
229 via the GasBench interface. No krypton interference (Schmitt et al., 2013) could
230 be determined in this setup. The repeatability for δD was generally better than 2
231 ‰ (reported as SD), based on consecutive analyses of reference air.

232 For $\delta^{13}\text{C}$, the CH₄ was injected from the cryofocus unit into a combustion oven
233 containing a nickel / nickel oxide wire catalyst at 1100 °C, where the CH₄ was
234 converted to CO₂ and H₂O. The resulting gas mixture passed a nafion dryer and a
235 10 m PoraPLOT Q column (5 °C) to eliminate interference from co-trapped
236 krypton (Schmitt et al., 2013) before entering the IRMS via the GasBench
237 interface. The repeatability of $\delta^{13}\text{C}$ was better than 0.07 ‰ (reported as SD),
238 based on consecutive analyses of reference air.

239 The typical measurement order during the Cabauw campaign was Ref $\delta^{13}\text{C}$ – Air
240 $\delta^{13}\text{C}$ – Ref δD – Air δD . A full measurement cycle took 84 min. On a regular basis,
241 pressurized air from a cylinder, applied as a target gas, was analyzed as a quality

242 control tool in order to monitor the long term stability of the analytical
243 technique. The CH₄ mole fraction and isotopic composition in ambient air and
244 target gas were calculated using an interpolation of the reference air analyzed
245 before and afterwards. A custom made LabView software program (National
246 Instruments Corp., USA) was used to control and log the temperature of the
247 traps, the valve switching and the flow setpoints of the MFCs.

248 **2.3.3. IRMS system isotope calibration**

249 The isotope calibration of the IRMS system was based on a reference air cylinder
250 that contains ambient air collected at the IMAU in 2014, with 1888 nmol/mol of
251 CH₄ and isotope values of $\delta^{13}\text{C} = (-47.89 \pm 0.05) \text{‰}$ and $\delta\text{D} = (-88.08 \pm 1.1) \text{‰}$.
252 The isotope calibration scale is based on the reference scale that was described
253 in detail in Brass and Röckmann (2010). We used the average of the reference air
254 measurement before and after the sample air measurement to calculate the mole
255 fraction and δ values. The linear response of the analytical system (independence
256 of the δ value on the amount of CH₄ analyzed) was verified by injecting various
257 volumes of reference air up to a volume equivalent to 2700 nmol/mol.
258 Occasionally, the long-term stability of the system was checked by measuring 3
259 target cylinders with different CH₄ mole fractions and isotopic compositions. A
260 robust link of the isotopic composition to the international reference materials
261 VPDB and VSMOW has been established in the framework of the INGOS project
262 (Sperlich et al., 2016).

263 **2.4. QCLAS system**

264 The analytical procedure of the laser based measurement system involves two
265 steps: preconcentration of the CH₄ from 7.5 L of ambient air in a trace gas
266 extractor (TREX) by adsorption on HayeSep D (Eyer et al., 2014; Mohn et al.,
267 2010) and analysis of CH₄ isotopologues with a modified commercial QCLAS
268 (QCL-76-D, Aerodyne Inc., USA). Details on the development, optimization and
269 validation of the TREX-QCLAS system are given by Eyer et al. (2015).

270 The present manuscript comprises the first application of the TREX-QCLAS
271 system for in-situ analysis of CH₄ isotopologues at a field site for an extended
272 period of time. In comparison to the original setup, the heating power of the

273 polyimide foil on the cold trap was reduced to 60 W to increase its lifetime. Due
274 to the lower heating power, the duration of the desorption step had to be
275 extended, which led to an improved separation from residual bulk gases (e.g. N₂
276 and O₂). Lowering the O₂ enhancement in the gas matrix is also the main reason
277 for a lower offset in $\delta^{13}\text{C}$ of $(1.58 \pm 0.2) \text{ ‰}$, with respect to the MPI - scale, as
278 compared to 2.3 ‰ in previously published results (Eyer et al., 2015). The
279 offset was related to a higher O₂ mole fraction in the gas matrix after CH₄
280 preconcentration. One measurement cycle consisted of four consecutive
281 measurements of ambient air samples and one sample of pressurized air used as
282 a target gas, followed by a calibration phase and took around 4:30 hours. This
283 translates into an analysis time of 54 minutes per sample of ambient or
284 pressurized air.

285 A calibration gas (CG1, $(1200 \pm 50) \text{ } \mu\text{mol/mol}$ CH₄ in high purity synthetic air
286 (79.5% N₂ and 20.5% O₂), $\delta^{13}\text{C} = -(44.24 \pm 0.10) \text{ ‰}$, $\delta\text{D} = -(104.7 \pm 1.1) \text{ ‰}$) was
287 diluted with the same synthetic air to 688 $\mu\text{mol/mol}$ and analyzed between
288 every preconcentrated sample as an anchor to correct the measurements for
289 instrumental drift. A second calibration gas (CG2, $(1103.8 \pm 3.5) \text{ } \mu\text{mol/mol}$ CH₄,
290 $\delta^{13}\text{C} = -(36.13 \pm 0.10) \text{ ‰}$, $\delta\text{D} = -(180.6 \pm 1.1) \text{ ‰}$), diluted to a similar CH₄ mole
291 fraction of 681 $\mu\text{mol/mol}$ was used to calculate calibration factors for $\delta^{13}\text{C}$ and
292 δD values. Furthermore, gas cylinders of pressurized ambient air, referred to as
293 target gas (TG1, TG2), were frequently measured over the entire campaign to
294 determine and verify the repeatability of the measurement system, which was
295 found to be 0.28 ‰ and 1.7 ‰ for $\delta^{13}\text{C}$ and δD (1σ), respectively. Additional
296 adjustments in the preconcentration procedure and in the analytical routine for
297 isotope analysis improved the repeatability to 0.18 ‰ and 0.85 ‰ for $\delta^{13}\text{C}$ and
298 δD in the last month of the campaign. One example is the improved temperature
299 control of the trap during adsorption, which in turn stabilized the O₂ content in
300 the measuring gas and thereby reduced variations in $\delta^{13}\text{C}$ -CH₄.

301 The CH₄ isotopic composition of the calibration gases, as well as the target gases
302 (pressurized air, TG1, $(2639.5 \pm 0.6) \text{ nmol/mol}$ CH₄, $\delta^{13}\text{C} = -(46.48 \pm 0.10) \text{ ‰}$, δD
303 $= -(119.0 \pm 1.1) \text{ ‰}$, TG2, $(2659.8 \pm 0.6) \text{ nmol/mol}$ CH₄, $\delta^{13}\text{C} = -(45.87 \pm 0.10) \text{ ‰}$,
304 $\delta\text{D} = -(114.1 \pm 1.1) \text{ ‰}$) were determined by the Stable Isotope Laboratory at the

305 Max-Planck-Institute for Biogeochemistry. CH₄ mole fraction measurements
306 were linked to the WMO-X2004 calibration scale (Dlugokencky et al., 2005)
307 through calibration of the target gases against NOAA reference standards at
308 Empa.

309 **2.5. Modeling**

310 Two complementary atmospheric transport models (TM5, FLEXPART-COSMO),
311 both in combination with two different emissions inventories (TNO-MACC_2,
312 EDGAR/LPJ-WhyMe), were applied to support interpretation of the
313 measurements. The Eulerian tracer model TM5 simulated the distribution of CH₄
314 and ¹³CH₄ at global scale with a zoom on Europe at 1° x 1° resolution and
315 considered both the isotopic signatures of different sources and the fractionation
316 by different removal pathways of CH₄ in the atmosphere. The Lagrangian particle
317 dispersion model FLEXPART-COSMO, conversely, was run in backward mode at a
318 higher resolution of 0.06° x 0.06° but only over Europe. This model is better able
319 to represent the spatial variability of CH₄ sources in the near field of Cabauw but
320 it only simulated the contributions from the last 4 days of emissions within
321 Europe and not the large-scale background. Chemical loss of CH₄ was not
322 considered due to the short transport times between the sources and the
323 receptor point at Cabauw.

324 **2.5.1. TM5 modeling**

325 Simulations of atmospheric CH₄ and δ¹³C were performed using the global tracer
326 model TM5 (Krol et al., 2005). The Eulerian off-line model was driven by
327 meteorological fields from the European Centre for Medium Range Weather
328 Forecast (ECMWF) reanalysis project ERA-Interim (Dee et al., 2011), pre-
329 processed for use in TM5. For vertical transport due to moist convection we
330 made use of Era Interim archived convective mass fluxes, replacing the use of the
331 Tiedke scheme in Krol et al. (2005). The model was run at a horizontal resolution
332 of 6°x4° globally and 1°x1° inside a zoom domain covering Western Europe. The
333 model uses 25 hybrid sigma-pressure levels from the surface to top of
334 atmosphere.

335 Two parallel (forward) TM5 simulations were performed with CH₄ and ¹³CH₄ as
336 transported tracers. In the standard configuration, anthropogenic CH₄ emissions
337 were taken from EDGAR4.2 FT2010 (EDGAR, 2009), extrapolated to 2014 and
338 2015 using annual statistics from the Food and Agriculture Organization of the
339 United Nations (FAO) and the British Petroleum Company (BP), as described in
340 Houweling et al. (2014). For natural wetland emissions, an average of the
341 emission estimates derived by Spahni et al. (2011) for the period 2003-2008 was
342 taken, using the LPJ-WhyMe model. For a complete description of the CH₄
343 emissions (Table 1), see Monteil et al. (2013) and references therein. ¹³CH₄
344 emissions were derived from the CH₄ emissions using prescribed $\delta^{13}\text{C}$ source
345 signatures (Table 1). The emission inventory was built according to a double
346 constraint: 1st, each source signature must be chosen within its own uncertainty
347 interval, and 2nd, the resulting global average source signature must be
348 compatible with the global source signature that is inferred from the
349 observations (and that is known with a much better precision than the individual
350 source signatures) (Monteil et al., 2011). In a second set of simulations,
351 anthropogenic emissions in a regional domain centered on Cabauw were
352 replaced by emissions from the European TNO-MACC_2 inventory, which was
353 used as the standard inventory in the FLEXPART-COSMO simulations (see
354 below). Outside the regional domain covered by TNO-MACC_2, the EDGAR
355 emissions were used.

356 Atmospheric removal of CH₄ was modeled as described in Monteil et al. (2013),
357 using kinetic fractionation factors $\alpha = k(^{12}\text{C}) / k(^{13}\text{C})$ of $\alpha_{\text{OH}} = 1.0055$, $\alpha_{\text{Cl}} = 1.066$
358 and $\alpha_{\text{O}(1\text{D})} = 1.013$ for the reactions between CH₄ and OH (Sander et al., 2006), Cl
359 (Saueressig et al., 1995) and O(¹D) (Saueressig et al., 2000), respectively. The
360 simulations were initialized at steady state (obtained via a spin-up run) in 2005,
361 and simulations of the period 2005-2015 were used to calculate a realistic state
362 of the atmosphere at the start of the measurement campaigns, including the
363 imbalance between emissions and atmospheric CH₄ mixing ratio/isotopic
364 composition in 2014. Time series were extracted from model-simulated mole
365 fraction fields after interpolation to the horizontal coordinate and height of the
366 Cabauw tower air inlet.

367 **2.5.2. FLEXPART-COSMO modeling**

368 The Lagrangian Particle Dispersion Model (LPDM) FLEXPART (Stohl et al., 2005)
369 was used in a modified version coupled to the mesoscale numerical weather
370 forecast model COSMO (Baldauf et al., 2011) to simulate the regional
371 contribution of different source categories to the concentrations and isotopic
372 signatures of CH₄ at Cabauw. FLEXPART-COSMO was driven by hourly
373 operational analysis fields generated by the Swiss national weather service
374 MeteoSwiss for a domain covering entire western and central Europe from
375 Ireland, Denmark, and Poland in the north to Portugal and southern Italy in the
376 south with a horizontal resolution of approximately 7 km x 7 km and 60 vertical
377 levels. Every 3 hours, 50'000 particles (air parcels) were released from the
378 position of the inlet 20 m above surface and traced backward in time for 4 days
379 to compute the sensitivity of each 3-hourly measurement to upwind sources. The
380 corresponding source sensitivity maps or footprints (Seibert and Frank, 2004)
381 were multiplied with gridded CH₄ emissions to compute the mole fraction
382 enhancement above background expected from different sources. Emissions
383 were taken from the TNO-MACC_2 inventory for Europe representative of the
384 year 2009 and available at 0.125° x 0.0625° resolution (Kuenen et al., 2014) or,
385 alternatively, from the same version of EDGAR/LPJ-WhyMe inventory driving
386 TM5 at a resolution of 1° x 1°. Methane mole fractions were computed separately
387 for a number of SNAP (Standardized Nomenclature for Air Pollutants) source
388 categories with specific isotopic signatures as summarized in Table 2.

389 For the domain covered by the FLEXPART-COSMO simulations, which includes
390 most of western and central Europe, total anthropogenic emissions are 20.6 Tg
391 CH₄/yr in EDGAR and 18.3 Tg CH₄/yr in TNO-MACC, which corresponds to a
392 difference of 12.5%. CH₄ emissions from gas/oil production and distribution are
393 89% higher, CH₄ emissions from agriculture 19% lower and CH₄ emissions from
394 waste 12% higher in EDGAR than in TNO-MACC.

395 Source specific emissions were combined with isotopic signatures of the various
396 categories from Table 2 to derive mean $\delta^{13}\text{C}$ and δD isotopic signatures for the
397 CH₄ that was picked up by the air parcel along the trajectory.

398 **2.6. Interpretation of CH₄ isotope data**

399 **2.6.1. Data analysis by a Keeling plot technique**

400 The isotopic composition of CH₄ emissions were estimated using the Keeling plot
401 technique (Keeling, 1961; Pataki et al., 2003). This method allows the isotopic
402 signature of a single source process or the mean isotopic signature of combined
403 source processes that mix into a background reservoir to be determined from
404 the observed ambient isotopic composition and mole fraction. An implicit
405 assumption of the Keeling plot approach is that the isotopic composition and
406 mole fraction of the background reservoir and the isotopic composition of the
407 source or the combined source stay constant over the time range of the analysis.
408 This may not always apply as the relative contribution of individual CH₄ sources
409 or their isotopic signature may change over time

410 To exploit the high temporal resolution of our data, we applied a novel approach
411 of a moving Keeling plot (MKP) method. Data within a moving window of 12
412 hours were used to calculate the source isotopic composition. This window was
413 moved in 1-hour time steps over the data series. In addition, values for
414 background conditions within a 48-hour period, centered on the respective 12-
415 hour window, were included in the analysis. These background values were
416 chosen between 10:00 and 18:00 local time, because during this period a
417 convective boundary layer usually develops and hence local influence is weak;
418 pollution events with CH₄ mole fractions above 2100 nmol/mol were filtered out
419 additionally. For each time window, an orthogonal least squares fit was applied
420 to the δ values vs. the inverse CH₄ mole fractions and R² values were calculated.
421 A Keeling plot analysis only returns meaningful values for the source isotopic
422 composition if the variations in CH₄ mole fraction are significant and if the
423 emissions are from a source with a well-defined isotopic composition. Therefore,
424 two additional filters were applied: i) the mole fraction had to vary by more than
425 200 nmol/mol within each time window and ii) the R² of the fit had to be larger
426 than 0.8. If R² < 0.8, the 12 h interval was reduced consecutively by one hour to a
427 minimum of six hours until either the R² of the fit was > 0.8 or the number of
428 data points was lower than five. On average this technique accumulated 22 data
429 points per 12-h time window.

430 **3. Results**

431 **3.1. Overview of the field measurements at the Cabauw site**

432 The full record of the methane mole fraction and isotopic composition obtained
433 with the two measurement techniques at the CESAR site is shown in Fig. 2. The
434 IRMS system started with δD measurements first, and after 3 weeks delivered
435 both $\delta^{13}C$ and δD data. The TREX-QCLAS system started later and ran
436 continuously from mid-December to mid-January, and from mid-February to the
437 end of the campaign. Despite a number of interruptions mainly due to various
438 kinds of instrument malfunction, the combined time series of both techniques
439 shows a high temporal coverage with more than 2500 measurements performed
440 for both $\delta^{13}C$ and δD .

441 A qualitative inspection of the time series already conveys the obvious features
442 that will be discussed below in more detail: the methane mole fraction $\chi(CH_4)$
443 shows a large number of substantial increases above background level, and these
444 positive methane excursions are accompanied by negative excursions in the δ
445 values from the background level. Thus the additional methane is generally
446 depleted in both ^{13}C and D.

447 **3.2. Comparison of the two analytical techniques**

448 Before presenting a detailed analysis of the CH_4 isotopic composition in ambient
449 air, we compare the results obtained with the IRMS and QCLAS techniques in
450 order to evaluate their performance and to combine the results into one final
451 dataset. Although both systems measured air from the same intake line, the
452 sampling intervals could not be synchronized since both instruments operated in
453 different measurement cycles. A full measurement cycle (including measurement
454 of the reference gas) took 84 minutes for the IRMS system and 54 minutes for
455 the TREX-QCLAS system. The actual duration of the air sampling was 10 minutes
456 for the IRMS system and 15 minutes for the QCLAS system. So even if the systems
457 coincidentally started sampling at the same time, they never actually analyzed
458 exactly the same air mass. Consequently, differences between the systems
459 contain contributions from natural variability, random fluctuations due to
460 limited measurement precision, and system offsets.

461 Fig. 3 shows a comparison of the $\chi(CH_4)$, as well as $\delta^{13}C$ and δD values that were
462 obtained with the TREX-QCLAS and the IRMS technique. To visualize the possible

463 effect of time shifts, the size of the points corresponds to the proximity of the
464 sampling intervals. A total of 727, 333 and 277 measurement pairs for $\chi(\text{CH}_4)$,
465 $\delta^{13}\text{C}$ and δD , respectively, analyzed by both techniques were combined in this
466 way.

467 The mole fraction comparison shows good agreement along the 1:1 line but with
468 a large scatter, which has two contributions: i) instrumental noise, as the isotope
469 systems have a relatively large uncertainty for measurement of the mole fraction
470 compared to existing high-precision CH_4 analyzers, and ii) natural variability
471 associated with the sampling of different air masses as described above. The
472 second point is supported by the fact that the average difference in CH_4 mole
473 fractions between the two analytical techniques was larger for larger temporal
474 differences in the sampling intervals.

475 For the isotope intercalibration plots, the grey-black shading of the circles
476 indicates the difference in $\chi(\text{CH}_4)$ of the respective measurement pair analyzed
477 by both techniques. The overall difference between the measurements
478 conducted with the two systems (QCLAS-IRMS) is $(+0.25 \pm 0.04) \text{‰}$ for $\delta^{13}\text{C}$ and
479 $(-4.3 \pm 0.4) \text{‰}$ for δD (the stated errors are standard errors of the mean). The
480 mean offsets are slightly outside the WMO extended compatibility goals for $\delta^{13}\text{C}$
481 (0.2‰) and within the WMO extended compatibility goals for δD (5‰), as
482 indicated by the red dashed lines (WMO, 2014). Individual measurement pairs
483 can show significantly larger deviations for aforementioned reasons. Differences
484 between the two techniques are higher than expected as both laboratories refer
485 their measurements to MPI-BGC, who recently established a link between the
486 CH_4 isotopic composition and the international reference materials VPDB and
487 VSMOW, in the framework of the INGOS project (Sperlich et al., 2016). Therefore,
488 remaining differences can only be rationalized by uncertainties in propagating
489 the scale or by instrumental issues. The enhanced discrepancies for low δD - CH_4
490 values might originate from a non-linear response of one of the applied
491 analytical techniques. The mean offset values determined above were applied to
492 the QCLAS data to create one combined dataset with 2610 data points for $\delta^{13}\text{C}$
493 and 2673 data points for δD .

494 **3.3. FLEXPART-COSMO source attribution**

495 In FLEXPART-COSMO, the contributions of the individual source types are
496 simulated separately and added up to obtain the cumulative CH₄ mole fraction.
497 Fig. 4 shows these contributions in absolute (top) and relative terms (bottom).
498 According to the model, the relative contributions at the Cabauw site are quite
499 uniform, with agricultural sources accounting for more than 60%, waste (mostly
500 landfills) around 20–40%, and fossil sources between 0 and 40%. We note that
501 significant contributions from fossil sources are only detected episodically,
502 during several events that usually last a few days. Contributions from other
503 source categories are generally negligible at the Cabauw site.

504 **3.4. TM5 and FLEXPART-COSMO modeling including isotopes**

505 The TM5 model calculates the combined influence of the global methane sources
506 and sinks on CH₄ and δ¹³C at the Cabauw tower, and therefore the TM5 results
507 can be compared directly to the measured time series. For FLEXPART-COSMO, a
508 representative background mole fraction and isotopic signature needs to be
509 added for comparison with the observations. For simplicity we assumed a
510 constant background similar to the observed values for background conditions:
511 1930 nmol/mol for χ(CH₄) with δ¹³C = -47.1 ‰ and δD = -86 ‰.

512 Fig. 5 shows a comparison of these model-generated time series with the
513 measured data for the entire campaign. Both models capture the amplitude and
514 the temporal variability of χ(CH₄) well. Most of the methane pollution events
515 observed at the CESAR site are also present in the modeled time series and the
516 increase in χ(CH₄) is of a comparable size. In addition, the results of the TM5 and
517 the FLEXPART-COSMO model for CH₄ mole fractions agree relatively well with
518 each other (R²=0.69), in particular when both models are run with the same
519 inventory at the same coarse spatial resolution, i.e. with EDGAR/LPJ-WhyMe.

520 A few pronounced CH₄ events in Fig. 5 show larger differences between the
521 models. On 2 November, FLEXPART-COSMO simulates an emission signal that is
522 not captured by TM5. Unfortunately no measurements are available for this
523 event to decide on which model performs better. On 30 November TM5
524 simulates a CH₄ plume, which is absent in FLEXPART-COSMO, and this event is
525 also not supported by the measurements. The global model has the advantage

526 that it includes the influence of long-range transport. As expected, however, the
527 observed variability is predominantly influenced by local and regional emissions.
528 Regarding the time series of the δ values, both TM5 and FLEXPART-COSMO
529 qualitatively display the expected anti-correlations between CH_4 and $\delta^{13}\text{C}$.
530 However, the amplitude of the $\delta^{13}\text{C}$ variability is generally underestimated in the
531 model runs, especially when using the EDGAR inventory. In addition, the
532 modeled background level of $\delta^{13}\text{C}$ in TM5 is offset by up to 1 ‰, but this offset is
533 also present at clean background sites in the Northern hemisphere.

534 Using the TNO-MACC inventory in FLEXPART-COSMO results in better
535 agreement with the observed variability of $\delta^{13}\text{C}$. In TM5, the TNO-MACC
536 emissions reduce the amplitude of the CH_4 variability, which is explained by the
537 13% lower emissions in TNO-MACC compared with EDGAR. Furthermore, the
538 results of both models are consistent with the emissions being more depleted in
539 $\delta^{13}\text{C}$ in TNO-MACC than in EDGAR. The measurements indicate emissions that
540 are even more depleted in $\delta^{13}\text{C}$ than TNO-MACC values. These results suggest
541 that the fractional contribution of isotopically heavy fossil emissions is
542 overestimated in EDGAR, at least in the area sampled by Cabauw, although the
543 uncertainty in the assumed $\delta^{13}\text{C}$ source signatures could also contribute. For
544 instance, recent literature showed that landfill emissions from the UK are more
545 depleted in $^{13}\text{CH}_4$ due to the implementation of gas extraction systems (Zazzeri
546 et al., 2015).

547 The δD time series simulated with FLEXPART-COSMO using the TNO-MACC
548 inventory is in good agreement with the measurements. This further indicates
549 that TNO-MACC has a realistic source mixture, but the uncertainties in the mean
550 δD signature are too large to draw firm conclusions at this stage. Despite these
551 uncertainties, Fig. 5 clearly demonstrates how isotopic measurements highlight
552 differences between emission inventories, which would go unnoticed looking
553 only at CH_4 mole fractions. Additional information may be available from the
554 combination of both isotope signatures. For several of the CH_4 elevation events
555 shown in Fig. 5b, the relative changes in $\delta^{13}\text{C}$ and δD modeled with FLEXPART-
556 COSMO vary when using the two different inventories (TNO-MACC and EDGAR).
557 Some of the anomalies show differences pointing in the same direction for $\delta^{13}\text{C}$

558 and δD , and some others not. This suggests that δD provides additional
559 independent information, which will be discussed in more detail in Section 4.3
560 using a double isotope plot of the source signatures (Fig. 7). The benefit of the
561 high-resolution dual isotope measurements for validating emissions used in the
562 models will be investigated in Section 4.4.

563 **4. Discussion**

564 **4.1. Diurnal and synoptic variability**

565 A prominent feature of the high-resolution dataset is the pronounced diurnal
566 variability, with large increases in CH_4 mole fraction that occur often during the
567 night, due to the shallow planetary boundary layer. In addition, there are also
568 several synoptic (but much smaller) pollution events, where CH_4 mole fractions
569 stay above the unpolluted background level for several days. These elevations
570 are likely caused by synoptic scale advection of CH_4 plumes from other source
571 regions with a different source mix.

572 **4.2. Isotope identification of the mean CH_4 source**

573 In Fig. 6, the Keeling plot technique is applied to identify the mean isotopic
574 signatures ($\delta^{13}C$, δD) of the combined CH_4 emissions detected at the Cabauw site.
575 An orthogonal regression method was applied to determine the fit parameters.
576 This analysis yields well-defined mean isotopic signatures of the cumulative
577 source (the y-intercept of the regression analysis) of $\delta^{13}C = -(60.8 \pm 0.2) \text{‰}$ and
578 $\delta D = -(298 \pm 1) \text{‰}$. The inferred mean isotopic signature agrees well with
579 emission from ruminants, which are expected to be the main source of CH_4 in
580 this rural area. This is plausible, because the mean isotopic signature is largely
581 determined by the pronounced nighttime CH_4 elevations, which represent the
582 local emissions close to the tower. Also the source contributions modeled by
583 FLEXPART-COSMO suggest the dominant influence of agricultural emissions in
584 this rural area (Fig. 4). Interestingly, the mean isotopic signature for the much
585 smaller synoptic CH_4 variations of the background (red points in Fig. 6) is not
586 significantly different from the one for the complete dataset.

587 **4.3. Short-term variability**

588 Given the high temporal resolution of the dataset presented here, the isotope
589 variations can be interpreted in much more detail than the overall analysis
590 performed above. This allows identifying varying contributions of CH₄ sources
591 during different periods of the campaign. To do so, we applied a 12-hour Moving
592 Keeling Plot (MKP) method to the data, as described in Sect 2.6.1.

593 Fig. 7 summarizes the results of the MKP method in the form of a δD vs. $\delta^{13}C$ plot.
594 To combine $\delta^{13}C$ and δD measurements performed at different times, MKP
595 intercepts were averaged over 6 h intervals. Mean $\delta^{13}C$ signatures range between
596 -68 ‰ and -55 ‰ and mean δD signatures cover a relatively wide range
597 between -350 ‰ and -260 ‰, indicating emissions mainly from microbial
598 sources as derived from the cumulative Keeling plot analysis. During some
599 periods, however, elevated mean $\delta^{13}C$ and δD signatures reveal significant
600 additional contributions from waste and/or fossil emissions.

601 The colored symbols in Fig. 7 highlight the mean isotopic signatures of three 48 h
602 events (10-12, 16-18 and 22-24 March) that are discussed in more detail in the
603 following. For the event of 16-18 March, selected results of the 12 h MKP method
604 are displayed in Fig. 8, demonstrating the advantage of the high temporal
605 resolution data. It is possible to clearly distinguish variations in the mean
606 isotopic signatures during this event by variations in the y-axis intercepts. The
607 increase by about 6 ‰ for $\delta^{13}C$ and about 50 ‰ for δD , in the source isotopic
608 signature for this event, clearly indicates the gradually increasing contribution of
609 CH₄ from isotopically enriched sources, e.g. fossil fuel- or waste-related CH₄.

610 The temporal evolution of the observed source mixture is investigated in further
611 detail in Fig. 9, where the 16-18 March period (labeled as 2) is compared to two
612 other 48 h – periods (10-12 March; label 1, and 22-24 March; label 3), each with
613 significant diurnal CH₄ elevations. For event 1, the mean isotopic signatures
614 stayed rather constant at values around $\delta^{13}C = -63$ ‰ and $\delta D = -320$ ‰. These
615 values are typical for microbial emissions from an agricultural source and agree
616 well with the source contributions predicted for this period by the FLEXPART-
617 COSMO model.

618 Period 2 is characterized by much stronger isotopic change within the 48 h
619 period. The $\delta^{13}C$ signature increases to above -60 ‰ and the δD signature

620 increases to -240 ‰ by the end of the period (see Fig. 9). The double-isotope
621 plot in Fig. 7 shows that the change in δD during event 2b clearly points towards
622 fossil fuel sources, which provides independent support for the FLEXPART-
623 COSMO simulations, where the contributions from fossil-fuel- derived emissions
624 are higher for the second day.

625 For period 3, the mean $\delta^{13}\text{C}$ isotopic signatures increased during the 48 h by
626 about 2-3 ‰, whereas the δD signatures remained constant around -300 ‰. For
627 this period, the double isotope plot of Fig. 7 indeed shows a shift towards the
628 waste category. Also this observation is independently confirmed (at least
629 qualitatively) by the FLEXPART-COSMO model derived source attribution, which
630 indicates the largest fraction of waste-derived CH_4 for the first day and a small
631 addition of fossil CH_4 for the second day of event 3. These examples show that
632 even at a location like Cabauw, where one source category strongly dominates,
633 contributions from isotopically different sources can be identified if sufficiently
634 high-resolution dual isotope ratio data are available. We note that the
635 “directional” information in the double isotope plot is only available by
636 combining $\delta^{13}\text{C}$ and δD measurements. It would be much harder, if not
637 impossible, to detect an addition from fossil fuel- or landfill- derived CH_4 based
638 on $\delta^{13}\text{C}$ or δD data alone.

639 **4.4. Evaluation of emission databases with high temporal resolution CH_4** 640 **isotope data**

641 As described in Section 3.4, both the TM5 and the FLEXPART-COSMO model-
642 generated time series of CH_4 mole fractions show an adequate agreement with
643 the CH_4 measurements at the Cabauw site. Therefore, the comparison between
644 measurement data and the models can be used to evaluate the methane budget
645 in more detail. In this context, the measured and modeled isotopic composition
646 can be employed to assess the validity of emission inventories, EDGAR and TNO-
647 MACC, with respect to the magnitude and spatial distribution of source
648 categories. To compare the measured mean isotopic signatures to the model
649 results, the simulated isotope time series were linearly interpolated and
650 evaluated in the same way as the observations using the 12 h MKP method. This
651 analysis was performed for both models (TM5 and FLEXPART-COSMO), each

652 using both the EDGAR/LPJ-Why-Me and the TNO_MACC inventories.
653 Additionally, time series for the mean isotopic signatures were calculated
654 directly from FLEXPART-COSMO data, without using of the MKP method. This
655 direct method allowed an independent estimation of the mean isotopic
656 signatures and, thus, also provided an opportunity to evaluate the MKP method.

657 The statistics of the mean isotopic signatures from all four model-inventory
658 combinations are shown as histograms in Fig. 10, together with the
659 measurement-derived mean isotopic signatures and the directly derived
660 signatures from FLEXPART-COSMO modeling. A clear difference can be observed
661 between the mean isotopic signatures derived with the two different emission
662 inventories. Model runs with the EDGAR/LPJ-WhyMe emission inventory (red in
663 Fig. 10) tend to produce mean CH₄ isotopic signatures that are more enriched in
664 ¹³C and D than the model runs with TNO-MACC emissions. These differences are
665 very similar for the simulations using TM5 and FLEXPART-COSMO, suggesting
666 that differences originate from the emission inventories, rather than from
667 differences between the models themselves. The δ¹³C source signatures derived
668 from the measurements at the Cabauw tower are significantly more depleted
669 than any of the model-generated datasets. For δD, the mean isotopic signatures
670 using TNO-MACC emissions are relatively close to the measurements at Cabauw,
671 whereas the values using EDGAR emissions are much more enriched in CH₃D.

672 The high temporal resolution isotope data that are described in this paper thus
673 provide relevant information to further constrain models and/or emission
674 inventories, because the mean isotopic signatures can change rapidly. The
675 comparison of our first high-resolution isotope measurements at Cabauw to
676 model calculations clearly identify differences between the modeled inventories,
677 where the EDGAR inventory produced too enriched mean isotopic signatures
678 due to a higher contribution from fossil fuel sources. Similar differences in terms
679 of source contributions between EDGAR and TNO-MACC_2 were also reported by
680 Hiller et al. (2014) for Switzerland, and Henne et al. (2015) concluded that
681 natural gas emissions in Switzerland are likely overestimated in EDGAR.

682 **5. Conclusions and outlook**

683 The dual isotopic composition of CH₄ has been monitored for the first time with
684 high temporal resolution in an extended (5 months) field deployment with two
685 different instruments, an IRMS system and a QCLAS system, at the tall tower site
686 Cabauw, the Netherlands. The measurements of both instruments compare well
687 and can be combined to a time series of more than 2500 measurements for both
688 δ¹³C and δD. Using a moving Keeling plot technique, the mean isotopic signatures
689 of periods with significant CH₄ elevations can be derived with high temporal
690 resolution. The combination of δ¹³C and δD data provides strong constraints to
691 distinguish emissions from different source categories. Overall, CH₄ emissions at
692 the Cabauw tall tower are dominated by agricultural sources, but variations in
693 the mean isotopic signatures allow identification of events with increased
694 contributions from fossil fuel and waste sources, which can be used to validate
695 variations in the source mix, calculated using the FLEXPART-COSMO model.

696 The high-resolution isotope ratio measurements at Cabauw were compared to
697 model calculations that used two different emission inventories. When two very
698 different models (TM5 and FLEXPART-COSMO) used emissions from the EDGAR
699 inventory, they produced clearly too enriched mean isotopic signatures. The
700 modeled mean isotopic signatures were systematically more depleted and closer
701 to the measured ones when the TNO-MACC inventory was used. The differences
702 in the source signatures appear to originate from differences in the inventories
703 and not from differences in the models, which supports indications in the recent
704 literature that fossil fuel related emissions might be overestimated in EDGAR. We
705 note that measurements at Cabauw reflect only one limited region of the
706 European domain, and given the many degrees of freedom (transport, source
707 signatures used in the models, emission inventories), one single dataset is not
708 sufficient to make a final decision on the quality of the emission dataset. High
709 frequency analysis of δ¹³C- and δD at several locations would allow better
710 constraints on isotope source signatures and emissions in atmospheric models.
711 Our proof-of-concept study presented here using continuous high-resolution
712 techniques shows that this will be feasible in the future.

713

714 **Data availability**

715 The data used for the scientific analysis of this paper are available as
716 supplementary information to this paper and at
717 <https://www.projects.science.uu.nl/atmosphereclimate/Data.php>.

718

719 **Acknowledgements**

720 This project was funded by the European Community's Seventh Framework
721 Program (FP7/2007-2013) within the InGOS project under grant agreement No.
722 284274. Additional funding from the Swiss National Science Foundation (SNSF)
723 within grant No. 200021_134611 and TNA grants within INGOS is gratefully
724 acknowledged. The campaign at the Cabauw tall tower was made possible with
725 strong support from Marcel Brinkenberg (KNMI), Michel Bolder and Henk
726 Snellen (IMAU). We also thank Marco Weber (Empa) for assistance during
727 transport and setup of the TREX-QCLAS system at the CESAR site.

728 **Author contributions**

729 S.E. and C.vdV. carried out the isotope measurements at the Cabauw tower.
730 C.vdV., T.R. and W.A.B. developed the IRMS system. S.E., B.T., L.E. and J.M.
731 developed the TREX-QCLAS system. C.vdV., S.E., J.M., T.R., B.T., M.E.P., G.Z., D.L.,
732 E.G.N., and J.M.N. contributed to the Cabauw measurement campaign. G.M., S.H.
733 and D.B. performed the modeling with TM5 and FLEXPART-COSMO. S.E., T.R.,
734 J.M., B.T., E.H., D.B., G.M., S.H., C.vdV., M.E.P. and H.F. performed and contributed
735 to the data evaluation. S.E. produced the figures for the manuscript. T.R., S.E. and
736 J.M. wrote the manuscript with input from C.vdV., G.M., S.H., E.H., D.B., H.F. and
737 L.E. T.R., L.E. and J.M. designed the study as part of the INGOS project.

738 **Table 1** European CH₄ emissions and isotope source signatures ($\delta^{13}\text{C}$, δD) for the
 739 different source categories used in TM5.

Process	Yearly emissions (Europe, Tg CH ₄ /yr)	source signature $\delta^{13}\text{C}/\text{‰}$
Natural emissions	22.1	-59.2
Natural wetlands (1)		
<i>Peatland</i>	9.3	-68
<i>Wet mineral soils</i>	4.6	-65
<i>Inundated wetlands</i>	1.3	-60
Geological emissions (2)	6.5	-42
Termites (3)	0.4	-63
Anthropogenic emissions	45.3	-52.4
Biomass burning (4)	0,3	-23.6
Agriculture (5)		
<i>Domestic ruminants</i>	11	-64
<i>Manure</i>	3	-54
<i>Rice paddies</i>	0.17	-65
Energy sector (5)		
<i>Coal mining</i>	3.4	-47
<i>Oil production</i>	3	-42
<i>Gas production and distribution</i>	12	-42
<i>Oil combustion</i>	0.41	-32
Residential sector (5)	1.6	-32
Waste treatment (5)		
<i>Landfills</i>	9	-54
<i>Waste waters</i>	3	-50
Total	67.4	-54.6

740 (1) Spahni et al. (2011); (2) Etiope et al. (2008); (3) Sanderson et al. (1996); (4)
 741 GFED3/4 (<http://www.globalfiredata.org/>); (5) EDGAR4.2FT (EDGAR, 2010).

742

743 **Table 2** SNAP (Standardized Nomenclature for Air Pollutants) source categories
 744 and corresponding $\delta^{13}\text{C}$ and δD source signatures from the TNO-MACC_2
 745 inventory as used in FLEXPART-COSMO.

SNAP Category	Description	$\delta^{13}\text{C}/\text{‰}$	$\delta\text{D}/\text{‰}$
1	Energy industries, oil or gas production	-42	-175
2	Residential combustion	-32	-175
3+4	Industrial combustion and non-combustion processes	-60	-175
5	Extraction and distribution of fossil fuels including distribution of natural gas	-42	-175
7	Road transport	-20	-175
9	Waste including emissions from landfills	-54	-293
10	Agriculture including emissions from ruminants and manure management	-64	-319
6+8	Other emissions (negligible)	-42	-175

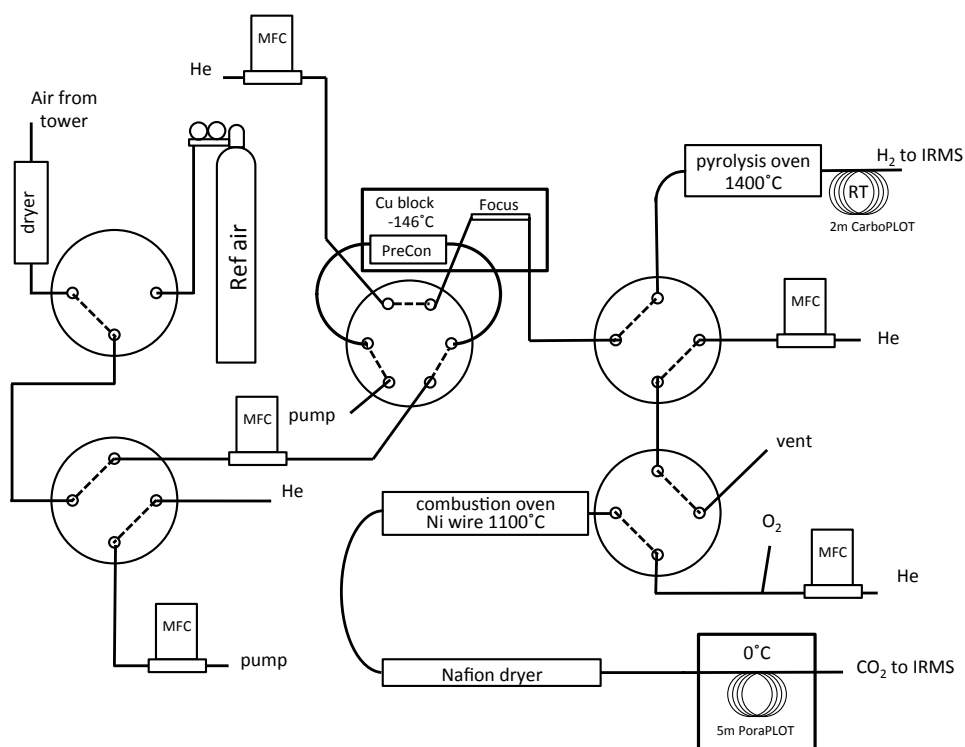
746

747 **Table 3.** Mean value and standard deviation of the histograms of the source
 748 isotopic composition shown in Fig. 10.

Model + Inventory	Method	$\delta^{13}\text{C}/\text{‰}$	$\delta\text{D}/\text{‰}$
Measurement data	MKP	-61.0 ± 2.8	-300 ± 22
TM5 + Edgar	MKP	-53.3 ± 1.1	
FLEXPART-COSMO + Edgar	MKP	-54.5 ± 1.6	-277 ± 10
FLEXPART-COSMO + Edgar	Direct	-53.4 ± 1.7	-269 ± 10
TM5 + TNO-MACC	MKP	-56.7 ± 0.8	
FLEXPART-COSMO + TNO-MACC	MKP	-57.6 ± 1.9	-294 ± 12
FLEXPART-COSMO + TNO-MACC	Direct	-57.2 ± 1.7	-289 ± 11

749

750 **Figures**

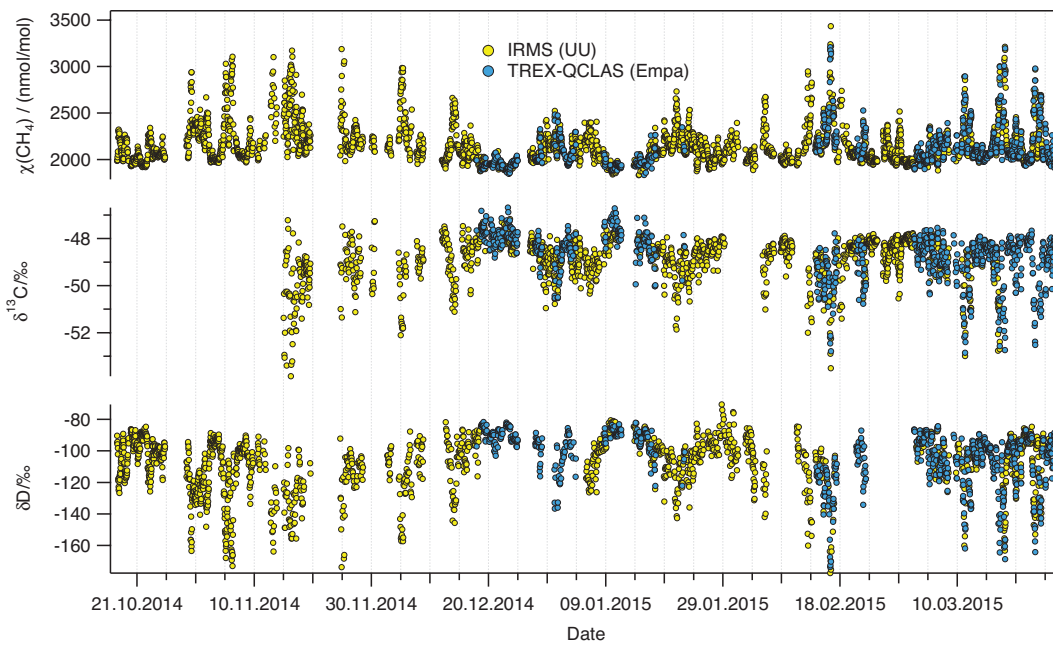


751 Fig. 1: Schematics of the pre-concentration and extraction system developed for
 752 the IRMS technique. MFC denotes mass flow controller. The 8-port valve through
 753 which the Ref air bottle was connected to the first selection valve is not shown to
 754 reduce complexity. For further description see the main text.

755

756

757

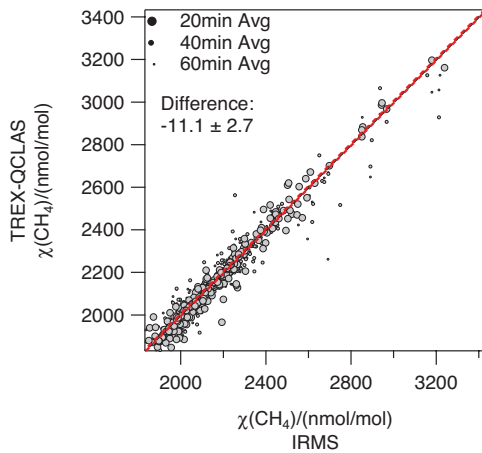


758

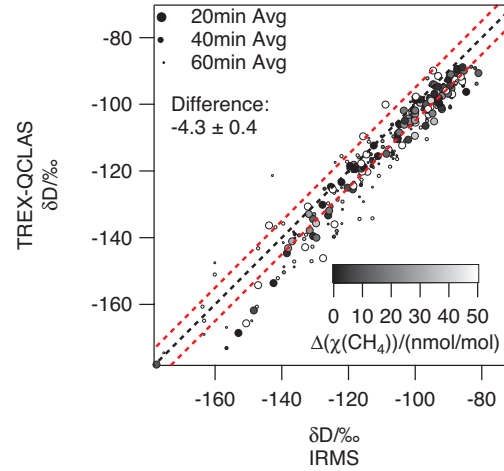
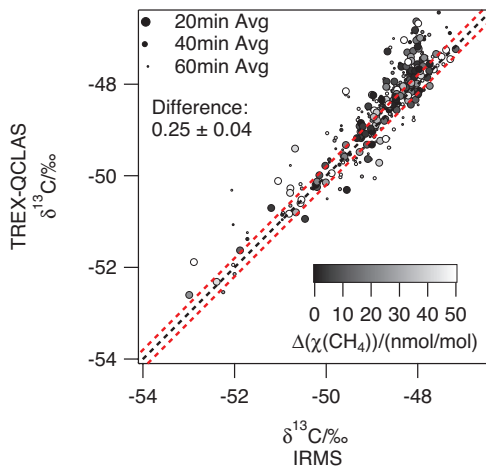
759 Fig. 2.: CH_4 mole fraction, $\chi(\text{CH}_4)$, and isotopic composition ($\delta^{13}\text{C}$, δD) measured
760 at the Cabauw tall tower from 17 October 2014 until 29 March 2015. Real-time
761 measurements by IRMS (Utrecht University) are indicated in yellow, TRES-
762 QCLAS (Empa) data in blue.

763

764



765



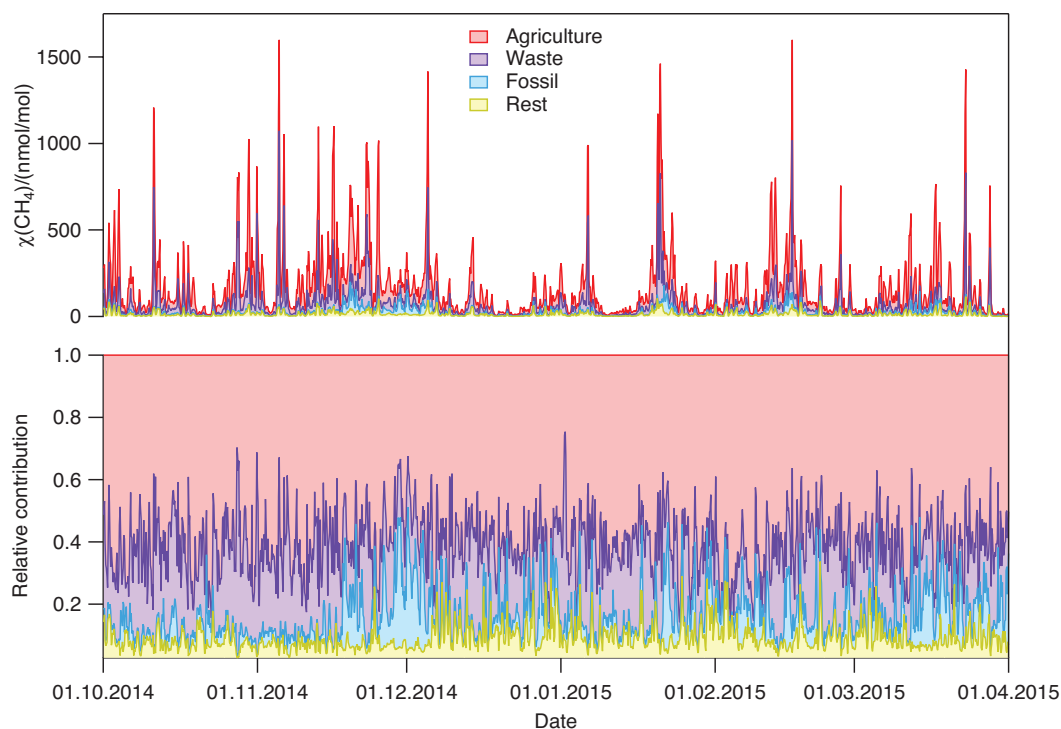
766

767

768

769 Fig. 3: Correlation diagrams for CH₄ mole fraction, $\delta^{13}\text{C}$ and δD analyzed with
770 IRMS (Utrecht University) and TREX-QCLAS (Empa). The dashed black lines are
771 1:1 lines, dashed red lines mark the extended WMO compatibility goals of ± 5
772 nmol/mol, ± 0.2 ‰ and ± 5 ‰ for CH₄ mole fraction, $\delta^{13}\text{C}$ and δD , respectively.
773 The temporal difference between IRMS and TREX-QCLAS sampling is indicated
774 by the point size (large: 20 min, medium: 40 min, small: 60 min). For $\delta^{13}\text{C}$ and δD ,
775 the differences in the CH₄ mole fraction of the measurements are represented by
776 the shading (black: identical mole fractions, white: 50 nmol/mol difference).

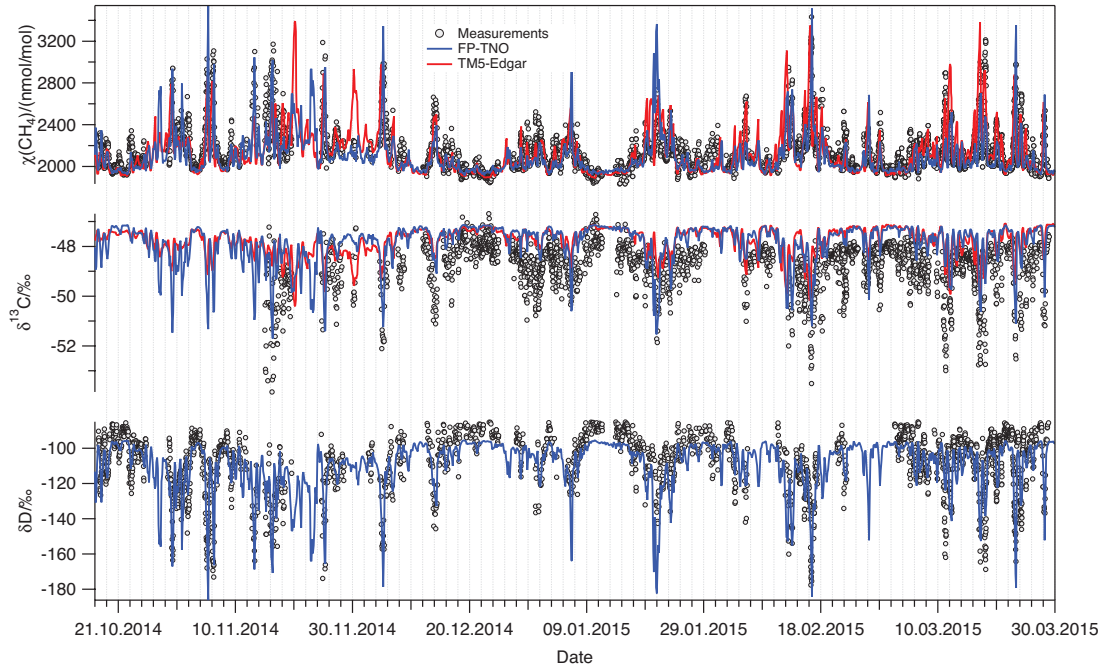
777



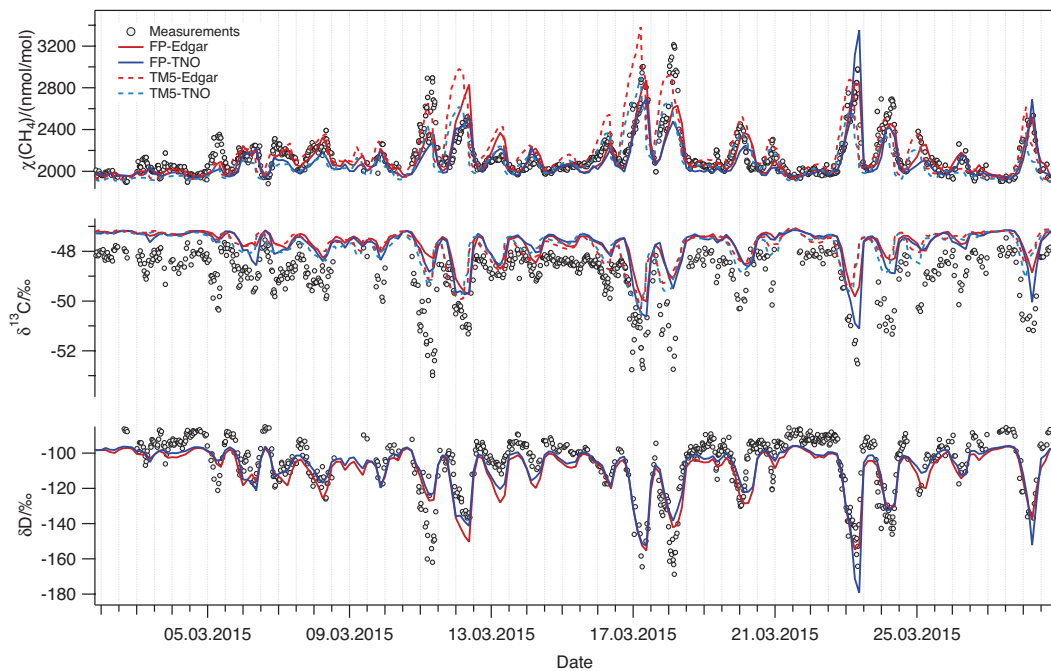
778

779 Fig. 4: Absolute (top) and relative (bottom) contributions of methane emissions
 780 that are picked up along the 4-day FLEXPART-COSMO trajectories during the
 781 campaign. The results shown are from the FLEXPART-COSMO simulations with
 782 the TNO-MACC inventory. They indicate major contributions of the following
 783 source categories: “agriculture” (mainly ruminants), “waste” (mainly landfills)
 784 and “fossil” (fugitive losses from coal, oil and natural gas production and from
 785 gas transportation and distribution) to the increase in CH_4 mole fractions at
 786 Cabauw. The category “rest” primarily represents residential CH_4 emissions.

787



788



789

790 Fig. 5: Comparison of the modeled and measured time series of CH₄ mole fraction
 791 and isotopic composition ($\delta^{13}\text{C}$ - and δD). Measurements are shown as circles and
 792 model results as lines. Top graph: two selected model configurations for the
 793 entire campaign: FLEXPART-COSMO using the TNO-MACC inventory (blue) and
 794 TM5 using the Edgar/Why-Me inventory (red). Bottom graph: Time series for
 795 March 2015 with all four model – inventory combinations. For δD , only the
 796 synthetic FLEXPART-COSMO results are available for comparison since TM5
 797 does not simulate δD .

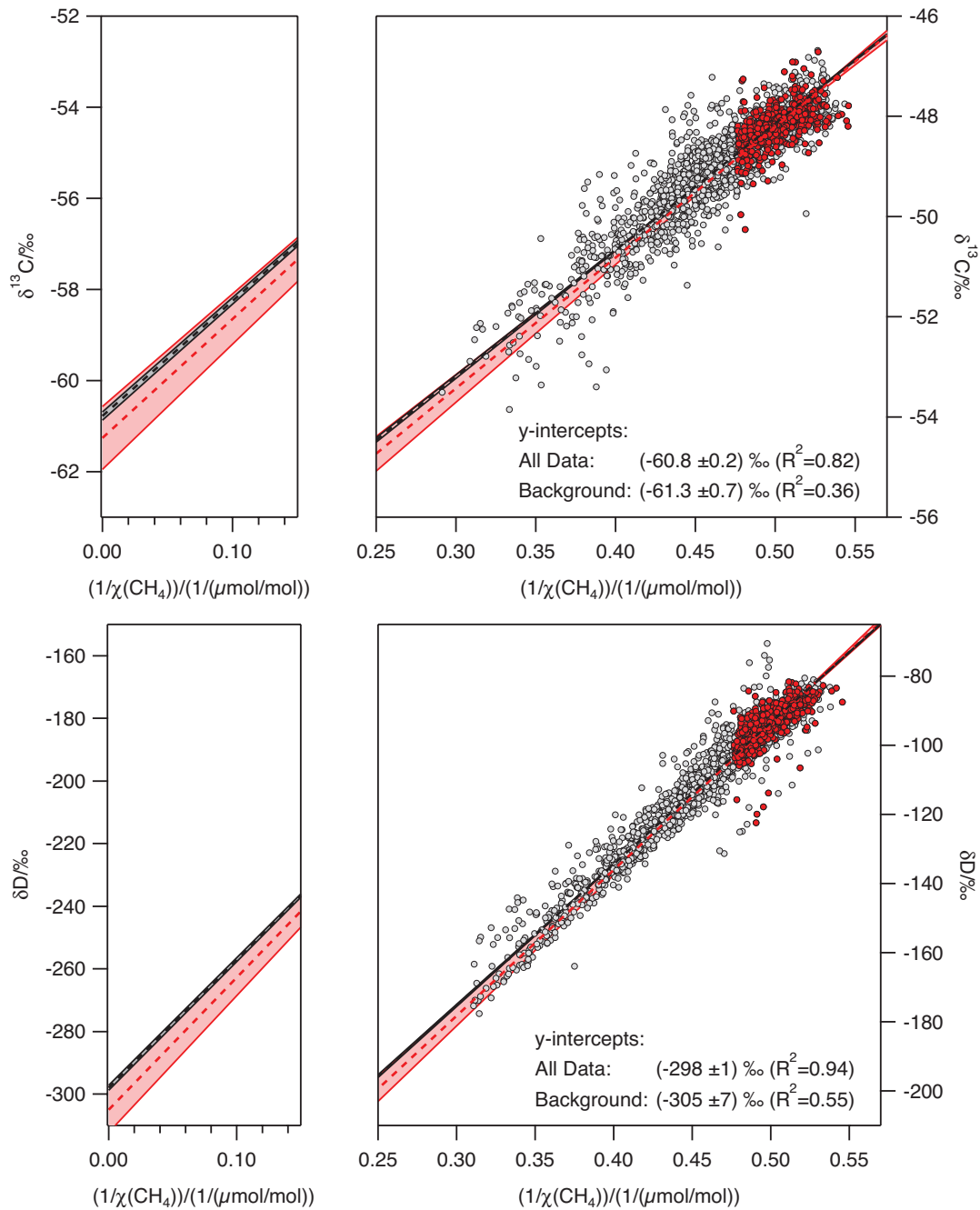
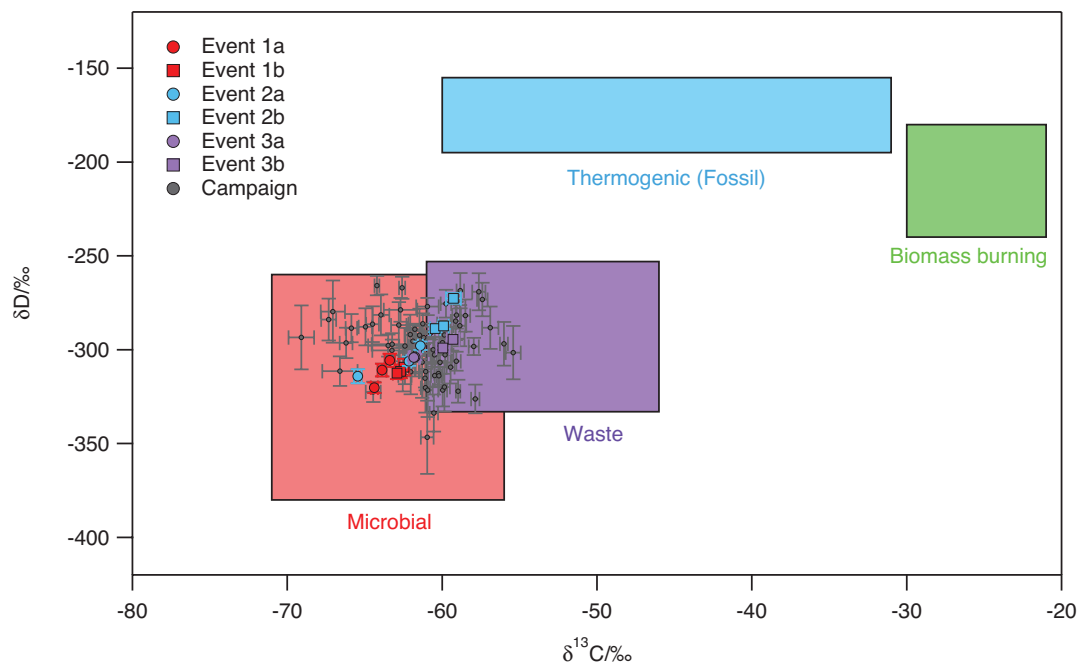


Fig. 6: Keeling plot of all data using an orthogonal regression method. The dashed line indicates the regression line and the shaded area the confidence interval taking into account the measurement uncertainties. The color code indicates all measured data (grey points) and daily background values (red points). Left panels show the region near the y-axis intercept.

806



807

808 Fig. 7: MKP intercepts of δD vs. $\delta^{13}C$. The colored areas indicate typical isotope
809 signatures for different source categories. Circles show the 6h-averaged source
810 signatures. Large colored symbols indicate data from the three events (event 1:
811 10th – 12th March, event 2: 16th – 18th March, event 3: 22nd to 24th March) that are
812 highlighted in Fig. 9. The labels a and b refer to day 1 and day 2 of the two-day
813 events, respectively. For the source signatures, the $\delta^{13}C$ values are taken from
814 Table 1 and the δD values from recent literature (Snoover et al., 2000; Rigby et al.,
815 2012).

816

817

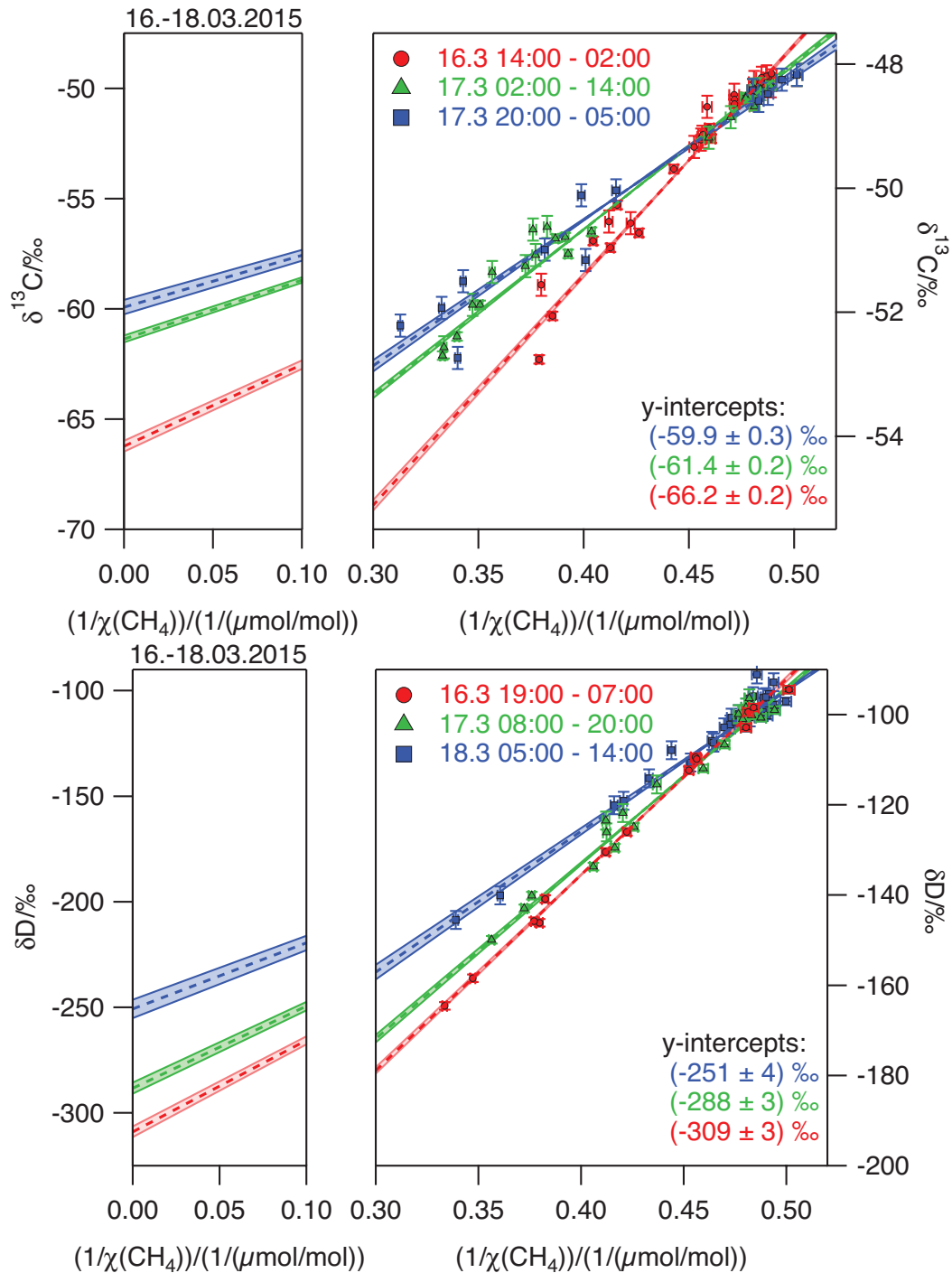
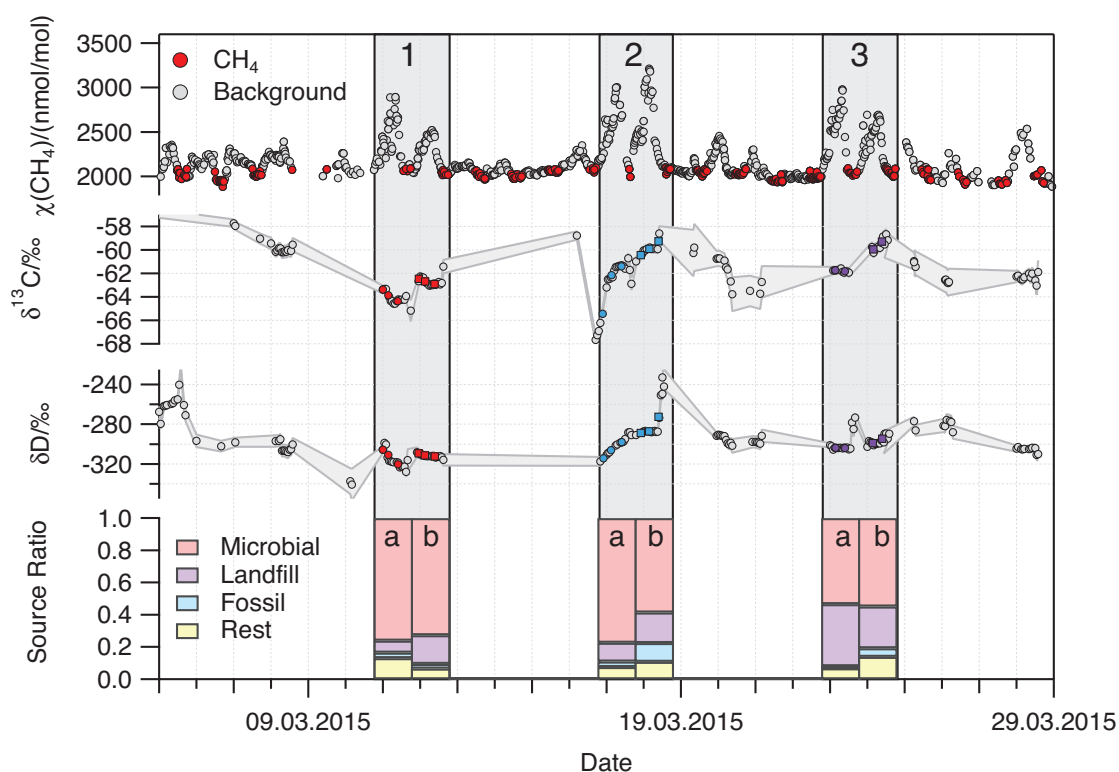


Fig. 8: Keeling plots for the period between 16 and 18 March, illustrating a rapid change in δ values over the course of hours, which is most probably related to a change from mainly ruminant derived CH_4 to a significant contribution of fossil and/or waste CH_4 . The dashed lines indicate the regression line, the shaded areas show the uncertainty (one standard deviation) of the regression line. Left panels show the region near the y-axis intercept. Times indicated are Central European Time (CET).



828

829 Fig. 9: Detailed analysis of three 2-day periods with large CH₄ elevations in
 830 March 2015. The top panel exhibits CH₄ mole fraction (grey) with background
 831 values in red (10:00-18:00, >2100 nmol/mol). The middle panels show the mean
 832 isotopic signatures ($\delta^{13}\text{C}$, δD) derived with the 12-h MKP method. The color-
 833 coding in the middle panels (red, light blue, purple) indicates characteristic
 834 contributions from different sources; red-microbial, light blue-fossil, purple-
 835 waste. For consistency, the same color-coding was chosen in Fig. 7. The bottom
 836 graph presents CH₄ source contributions as computed with the FLEXPART-
 837 COSMO model using the TNO-MACC inventory, averaged over 24 hours.

838

839

840

841

842

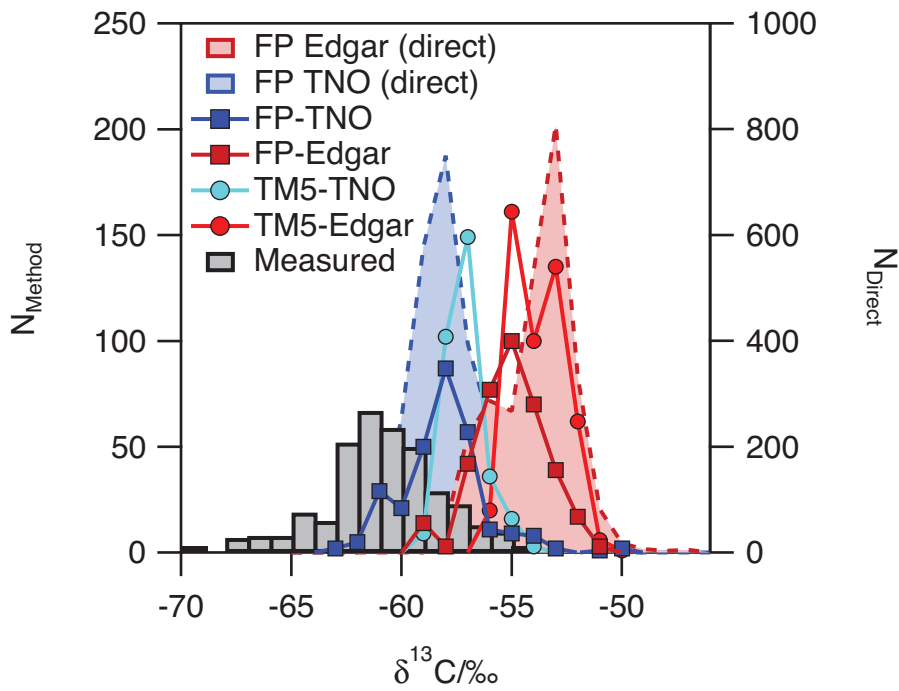
843

844

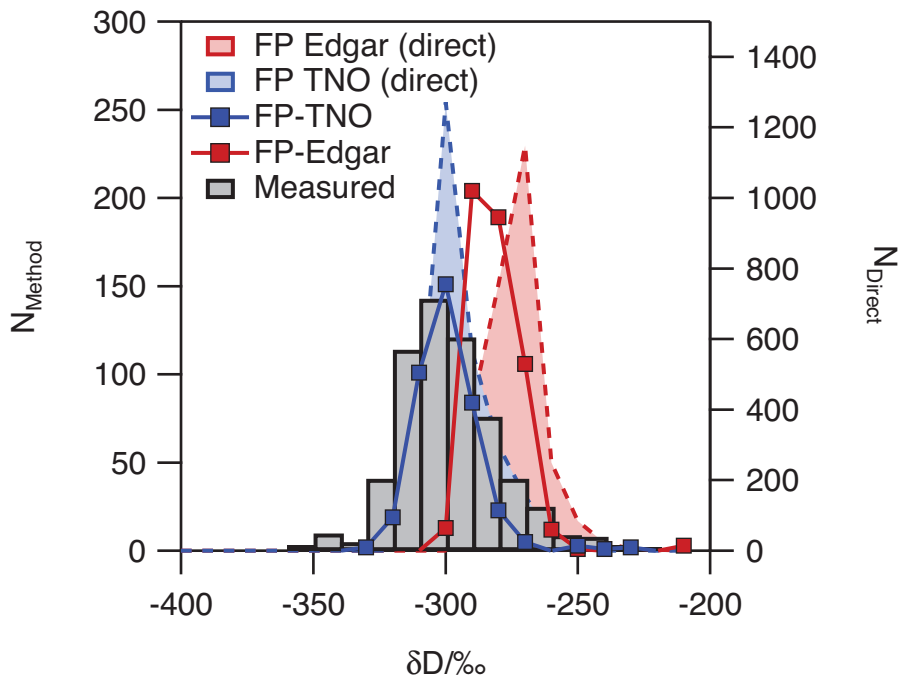
845

846

847



848



849

850 Fig. 10: Histograms of CH_4 isotopic source signatures at the CESAR site between
851 October 2014 and March 2015. Bin widths are 1 ‰ for $\delta^{13}\text{C}$ and 10 ‰ for δD .
852 Mean isotopic signatures are derived from measured data (grey bins),
853 FLEXPART-COSMO modeling (squares) as well as TM5 modeling (circles) using
854 the 12 h MKP method. Two different inventories, TNO-MACC (blue) and

855 Edgar/LPJ-Why-Me (red), were used. The shaded areas show histograms for the
856 “direct” source signatures that were picked up along the FLEXPART-COSMO
857 trajectory (right axis).

858 References

859 Baertschi, P.: Absolute ^{18}O content of Standard Mean Ocean Water, *Earth Planet.*
860 *Sci. Lett.*, 31, 341-344, 1976.

861 Baldauf, M., Seifert, A., Förstner, J., Majewski, D., Raschendorfer, M., and
862 Reinhardt, T.: Operational Convective-Scale Numerical Weather Prediction with the
863 COSMO Model: Description and Sensitivities, *Monthly Weather Review*, 139, 3887–
864 3905, doi:3810.1175/MWR-D-3810-05013.05011, 2011.

865 Beck, V., Chen, H. L., Gerbig, C., Bergamaschi, P., Bruhwiler, L., Houweling, S.,
866 Röckmann, T., Kolle, O., Steinbach, J., Koch, T., Sapart, C. J., van der Veen, C.,
867 Frankenberg, C., Andreae, M. O., Artaxo, P., Longo, K. M., and Wofsy, S. C.:
868 Methane airborne measurements and comparison to global models during BARCA, *J.*
869 *Geophys. Res.*, 117, D15310, doi:15310.11029/12011JD017345, 2012.

870 Bergamaschi, P., Brenninkmeijer, C. A. M., Hahn, M., Röckmann, T., Scharffe,
871 D. H., Crutzen, P. J., Elansky, N. F., Belikov, I. B., Trivett, N. B. A., and Worthy, D.
872 E. J.: Isotope analysis based source identification for atmospheric CH_4 and CO across
873 Russia using the Trans-Siberian railroad, *J. Geophys. Res.*, 103, D7, 8227-8235, DOI:
874 8210.1029/8297JD03738, 1998a.

875 Bergamaschi, P., Houweling, S., Segers, A., Krol, M., Frankenberg, C.,
876 Scheepmaker, R. A., Dlugokencky, E., Wofsy, S. C., Kort, E. A., Sweeney, C.,
877 Schuck, T., Brenninkmeijer, C., Chen, H., Beck, V., and Gerbig, C.: Atmospheric
878 CH_4 in the first decade of the 21st century: Inverse modeling analysis using
879 SCIAMACHY satellite retrievals and NOAA surface measurements, *J Geophys Res-*
880 *Atmos*, 118, 7350–7369, doi:7310.1002/jgrd.50480, 2013.

881 Bergamaschi, P., Lubina, C., Königstedt, R., Fischer, H., Veltkamp, A. C., and
882 Zwaagstra, O.: Stable isotopic signatures ($\delta^{13}\text{C}$, δD) of methane from European
883 landfill sites, *J. Geophys. Res.*, 103, 8251-8265, doi 8210.1029/8298jd00105, 1998b.

884 Bergamaschi, P., Schupp, M., and Harris, G. W.: High-precision direct
885 measurements of $^{13}\text{CH}_4/^{12}\text{CH}_4$ and $\text{CH}_3\text{D}/^{12}\text{CH}_4$ ratios in atmospheric methane
886 sources by means of a long-path tunable diode laser absorption spectrometer, *Appl.*
887 *Opt.*, 33, No.33, 7704-7716, 1994.

888 Bock, M., Schmitt, J., Behrens, M., Moller, L., Schneider, R., Sapart, C., and
889 Fischer, H.: A gas chromatography/pyrolysis/isotope ratio mass spectrometry system
890 for high-precision δD measurements of atmospheric methane extracted from ice cores,
891 *Rap. Commun. Mass Spectrom.*, 24, 621-633, 2010.

892 Brand, W. A., Rothe, M., Sperlich, P., Strube, M., and Wendeberg, M.:
893 Automated simultaneous measurement of the $\delta^{13}\text{C}$ and $\delta^2\text{H}$ values of methane and the
894 $\delta^{13}\text{C}$ and $\delta^{18}\text{O}$ values of carbon dioxide in flask air samples using a new multi cryo-
895 trap/gas chromatography/isotope ratio mass spectrometry system, *Rapid Commun.*
896 *Mass Spectrom.*, 30, 1523-1539, doi: 1510.1002/rcm.7587, 2016.

897 Brass, M. and Röckmann, T.: Continuous-flow isotope ratio mass spectrometry
898 method for carbon and hydrogen isotope measurements on atmospheric methane,
899 *Atmos. Meas. Tech.*, 3, 1707-1721, 2010.

900 Brennkmeijer, C. A. M., Lowe, D. C., Manning, M. R., Sparks, R. J., and
901 Velthoven, P. F. J. v.: The ^{13}C , ^{14}C , and ^{18}O isotopic composition of CO , CH_4 and
902 CO_2 in the higher southern latitudes lower stratosphere, *J. Geophys. Res.*, 100,
903 26,163-126,172, 1995.

904 Bruhwiler, L., Dlugokencky, E., Masarie, K., Ishizawa, M., Andrews, A., Miller,
905 J., Sweeney, C., Tans, P., and Worthy, D.: CarbonTracker- CH_4 : an assimilation
906 system for estimating emissions of atmospheric methane, *Atmos. Chem. Phys.*, 14,
907 8269-8293, 2014.

908 Craig, H.: Isotopic standards for carbon and oxygen and correction factors for
909 mass-spectrometric analysis of carbon dioxide, *Geochim. Cosmochim. Acta*, 12, 133-
910 149, 1957.

911 Dee, D. P., Uppala, S. M., Simmons, A. J., Berrisford, P., Poli, P., and al., e.: The
912 ERA-Interim reanalysis: configuration and performance of the data assimilation
913 system, *Quart. J. Roy. Meteor. Soc.*, 553-579, 2011.

914 Dlugokencky, E. J., Bruhwiler, L., White, J. W. C., Emmons, L. K., Novelli, P.
915 C., Montzka, S. A., Masarie, K. A., Lang, P. M., Crotwell, A. M., Miller, J. B., and
916 Gatti, L. V.: Observational constraints on recent increases in the atmospheric CH_4
917 burden, *Geophys. Res. Lett.*, 36, L18803, doi 18810.11029/12009gl039780, 2009.

918 Dlugokencky, E. J., Dutton, E. G., Novelli, P. C., Tans, P. P., Masarie, K. A.,
919 Lantz, K. O., and Madronich, S.: Changes in CH_4 and CO growth rates after the
920 eruption of Mt. Pinatubo and their link with changes in tropical tropospheric UV flux,
921 *Geophys. Res. Lett.*, 23, 2761-2764, 1996.

922 Dlugokencky, E. J., Masarie, K. A., Lang, P. M., and Tans, P. P.: Continuing
923 decline in the growth rate of the atmospheric methane burden, *Nature*, 393, 447-450,
924 1998.

925 Dlugokencky, E. J., Myers, R. C., Lang, P. M., Masarie, K. A., Crotwell, A. M.,
926 Thoning, K. W., Hall, B. D., Elkins, J. W., and Steele, L. P.: Conversion of NOAA
927 atmospheric dry air CH_4 mole fractions to a gravimetrically prepared standard scale, *J.*
928 *Geophys. Res.*, 110, D18306, Doi 18310.11029/12005jd006035, 2005.

929 EDGAR: European Commission, Joint Research Centre (JRC)/Netherlands
930 Environmental Assessment Agency (PBL). , Emission Database for Global
931 Atmospheric Research (EDGAR), Version 4.2. , 2010. Available at
932 <http://edgar.jrc.ec.europa.eu>., 2010.

933 EDGAR: European Commission, Joint Research Centre (JRC)/Netherlands
934 Environmental Assessment Agency (PBL). Emission Database for Global
935 Atmospheric Research (EDGAR), release version 4.2.
936 <http://edgar.jrc.ec.europa.eu>., 2009.

937 Etheridge, D. M., Steele, L. P., Francey, R. J., and Langenfelds, R. L.:
938 Atmospheric methane between 1000 AD and present: Evidence of antropogenic
939 emissions and climatic variability, *J. Geophys. Res.*, 103, 15979-15993, 1998.

940 Etiope, G., Lassey, K. R., Klusman, R. W., and Boschi, E.: Reappraisal of the
941 fossil methane budget and related emission from geologic sources, *Geophys. Res.*
942 *Lett.*, 35, 2008.

943 Eyer, S. and al, e.: Real-time analysis of $\delta^{13}\text{C}$ - and δD - CH_4 in ambient air with
944 laser spectroscopy: Method development and first intercomparison results., *Atmos.*
945 *Meas. Tech. Discuss.*, 8, 8925-8970, 2015.

946 Eyer, S., Stadie, N. P., Borgschulte, A., Emmenegger, L., and Mohn, J.: Methane
947 preconcentration by adsorption: a methodology for materials and conditions selection,
948 *Adsorption-Journal of the International Adsorption Society*, 20, 657-666, 2014.

949 Ferretti, D., Miller, J., White, J., Etheridge, D., Lassey, K., Lowe, D., Allan, B.,
950 MacFarling, C., Dreier, M., Trudinger, C., and Ommen, T. v.: Unexpected changes to
951 the global methane budget over the past 2000 years, *Science*, 309, 1714-1717, 2005.

952 Fischer, H., Behrens, M., Bock, M., Richter, U., Schmitt, J., Loulergue, L.,
953 Chappellaz, J., Spahni, R., Blunier, T., Leuenberger, M., and Stocker, T. F.: Changing
954 boreal methane sources and constant biomass burning during the last termination,
955 *Nature*, 452, 864-867, 2008.

956 Gros, V., Brenninkmeijer, C. A. M., Jöckel, P., Kaiser, J., Lowry, D., Nisbet, E.
957 G., O'Brian, P., Röckmann, T., and Warwick, N.: Isotope signatures of trace gas
958 sources. In: *Emissions Of Atmospheric Trace Compounds*, Granier, C., Artaxo, P.,
959 and Reeves, C. E. (Eds.), *Advances in Global Change Research*, Kluwer Academic
960 Pub., Paris, 2004.

961 Henne, S., Brunner, D., Oney, B., Leuenberger, M., Eugster, W., Bamberger, I.,
962 Meinhardt, F., Steinbacher, M., and Emmenegger, L.: Validation of the Swiss
963 methane emission inventory by atmospheric observations and inverse modelling,
964 *Atmos. Chem. Phys. Discuss.*, 2015. 35417-35484, doi:35410.35194/acpd-35415-
965 35417-32015, 2015.

966 Hiller, R. V., Bretscher, D., DelSontro, T., Diem, T., Eugster, W., Henneberger,
967 R., Hobi, S., Hodson, E., Imer, D., Kreuzer, M., Künzle, T., Merbold, L., Niklaus, P.
968 A., Rihm, B., Schellenberger, A., Schroth, M. H., Schubert, C. J., Siegrist, H., Stieger,
969 J., Buchmann, N., and Brunner, D.: Anthropogenic and natural methane fluxes in
970 Switzerland synthesized within a spatially explicit inventory, *Biogeosciences*, 11,
971 1941-1959, doi:1910.5194/bg-1911-1941-2014, 2014.

972 Houweling, S., Krol, M., Bergamaschi, P., Frankenberg, C., Dlugokencky, E. J.,
973 Morino, I., Notholt, J., Sherlock, V., Wunch, D., Beck, V., Gerbig, C., Chen, H., Kort,
974 E. A., Röckmann, T., and Aben, I.: A multi-year methane inversion using
975 SCIAMACHY, accounting for systematic errors using TCCON measurements,
976 *Atmos. Chem. Phys.*, 14, 3991-4012, 2014.

977 Houweling, S., van der Werf, G. R., Goldewijk, K. K., Röckmann, T., and Aben,
978 I.: Early anthropogenic CH₄ emissions and the variation of CH₄ and ¹³CH₄ over the
979 last millennium, *Global Biogeochem Cy*, 22, 2008.

980 Kawagucci, S., Kobayashi, M., Hattori, S., Yamada, K., Ueno, Y., Takai, K., and
981 Yoshida, N.: Hydrogen isotope systematics among H₂-H₂O-CH₄ during the growth of
982 the hydrogenotrophic methanogen *Methanothermobacter thermoautotrophicus* strain
983 Delta H, *Geochim Cosmochim Acta*, 142, 601-614, 2014.

984 Keeling, C. D.: The Concentration and Isotopic Abundances of Carbon Dioxide
985 in Rural and Marine Air, *Geochim. Cosmochim. Acta*, 24, 277-298, 1961.

986 Khalil, M. A. K., Butenhoff, C. L., and Rasmussen, R. A.: Atmospheric methane:
987 Trends and cycles of sources and sinks, *Environmental Science & Technology*, 41,
988 2131-2137, 2007.

989 Kirschke, S., Bousquet, P., Ciais, P., Saunois, M., Canadell, J. G., Dlugokencky,
990 E. J., Bergamaschi, P., Bergmann, D., Blake, D. R., Bruhwiler, L., Cameron-Smith,
991 P., Castaldi, S., Chevallier, F., Feng, L., Fraser, A., Heimann, M., Hodson, E. L.,
992 Houweling, S., Josse, B., Fraser, P. J., Krummel, P. B., Lamarque, J. F., Langenfelds,
993 R. L., Le Quere, C., Naik, V., O'Doherty, S., Palmer, P. I., Pison, I., Plummer, D.,

994 Poulter, B., Prinn, R. G., Rigby, M., Ringeval, B., Santini, M., Schmidt, M., Shindell,
995 D. T., Simpson, I. J., Spahni, R., Steele, L. P., Strode, S. A., Sudo, K., Szopa, S., van
996 der Werf, G. R., Voulgarakis, A., van Weele, M., Weiss, R. F., Williams, J. E., and
997 Zeng, G.: Three decades of global methane sources and sinks, *Nat Geosci*, 6, 813-823,
998 2013.

999 Klevenhusen, F., Bernasconi, S. M., Kreuzer, M., and Soliva, C. R.: Experimental
1000 validation of the Intergovernmental Panel on Climate Change default values for
1001 ruminant-derived methane and its carbon-isotope signature, *Anim Prod Sci*, 50, 159-
1002 167, 2010.

1003 Krol, M., Houweling, S., Bregman, B., van den Broek, M., Segers, A., van
1004 Velthoven, P., Peters, W., Dentener, F., and Bergamaschi, P.: The two-way nested
1005 global chemistry-transport zoom model TM5: algorithm and applications, *Atmos.*
1006 *Chem. Phys.*, 5, 417-432, 2005.

1007 Kuenen, J. J. P., Visschedijk, A. J. H., Jozwicka, M., and van der Gon, H. A. C.
1008 D.: TNO-MACC_II emission inventory; a multi-year (2003-2009) consistent high-
1009 resolution European emission inventory for air quality modelling, *Atmos. Chem.*
1010 *Phys.*, 14, 10963-10976, 2014.

1011 Lassey, K. R., Lowe, D. C., Brenninkmeijer, C. A. M., and Gomez, A. J.:
1012 Atmospheric Methane and its Carbon Isotopes in the Southern Hemisphere: their
1013 Time Series and an Instructive Model, *Chemosphere*, 26, 95-109, 1993.

1014 Lassey, K. R., Lowe, D. C., and Manning, M. R.: The trend in atmospheric
1015 methane $\delta^{13}\text{C}$ implications for isotopic constraints on the global methane budget,
1016 *Global Biogeochem Cy*, 14, 41-49, 2000.

1017 Loulergue, L., Schilt, A., Spahni, R., Masson-Delmotte, V., Blunier, T., Lemieux,
1018 B., Barnola, J. M., Raynaud, D., Stocker, T. F., and Chappellaz, J.: Orbital and
1019 millennial-scale features of atmospheric CH_4 over the past 800,000 years, *Nature*,
1020 453, 383-386, 2008.

1021 Lowe, D. C., Brenninkmeijer, C. A. M., Brailsford, G. W., Lassey, K. R., Gomez,
1022 A. J., and Nisbet, E. G.: Concentration and ^{13}C Records of Atmospheric Methane in
1023 New-Zealand and Antarctica - Evidence for Changes in Methane Sources, *J. Geophys.*
1024 *Res.*, 99, 16913-16925, 1994.

1025 MacFarling Meure, C., Etheridge, D., Trudinger, C., Steele, P., Langenfelds, R.,
1026 Ommen, T. v., Smith, A., and Elkins, J.: Law Dome CO_2 , CH_4 and N_2O ice core
1027 records extended to 2000 years BP *Geophys. Res. Lett.*, 33, L14810,
1028 doi:14810.11029/12006GL026152 2006.

1029 Merritt, D. A., Brand, W. A., and Hayes, J. M.: Isotope-ratio-monitoring gas
1030 chromatography-mass spectrometry: methods for isotopic calibration, *Org. Geochem.*,
1031 21 No. 6/7, 573-583, 1994.

1032 Merritt, D. A., Hayes, J. M., and Des Marais, D. J.: Carbon isotopic analysis of
1033 atmospheric methane by isotope-ratio-monitoring gas chromatography-mass
1034 spectrometry, *J. Geophys. Res.*, 100 D, 1317-1326, 1995.

1035 Mohn, J., Guggenheim, C., Tuzson, B., Vollmer, M. K., Toyoda, S., Yoshida, N.,
1036 and Emmenegger, L.: A liquid nitrogen-free preconcentration unit for measurements
1037 of ambient N_2O isotopomers by QCLAS, *Atmos Meas Tech*, 3, 609-618, 2010.

1038 Mohn, J., Tuzson, B., Manninen, A., Yoshida, N., Toyoda, S., Brand, W. A., and
1039 Emmenegger, L.: Site selective real-time measurements of atmospheric N_2O
1040 isotopomers by laser spectroscopy, *Atmos Meas Tech*, 5, 1601-1609, 2012.

1041 Monteil, G., Houweling, S., Dlugokenky, E. J., Maenhout, G., Vaughn, B. H.,
1042 White, J. W. C., and Röckmann, T.: Interpreting methane variations in the past two
1043 decades using measurements of CH₄ mixing ratio and isotopic composition, *Atmos.*
1044 *Chem. Phys.*, 11, 9141-9153, 2011.

1045 Monteil, G., Houweling, S., Guerlet, S., Schepers, D., Frankenberg, C.,
1046 Scheepmaker, R., Aben, I., Butz, A., Hasekamp, O., Landgraf, J., Wofsy, S. C., and
1047 Röckmann, T.: Intercomparison of 15 months inversions of GOSAT and
1048 SCIAMACHY CH₄ retrievals, *J. Geophys. Res.*, 118, 11807-11823,
1049 doi:10.1029/2013JD019760, 2013.

1050 Nisbet, E. G., Dlugokenky, E. J., and Bousquet, P.: Methane on the rise—again,
1051 *Science*, 343, 493-495, 2014.

1052 Pataki, D. E., Ehleringer, J. R., Flanagan, L. B., Yakir, D., Bowling, D. R., Still,
1053 C. J., Buchmann, N., Kaplan, J. O., and Berry, J. A.: The application and
1054 interpretation of Keeling plots in terrestrial carbon cycle research, *Global*
1055 *Biogeochem Cy*, 17, 1022, doi:10.1029/2001GB001850, 2003.

1056 Peltola, O., Hensen, A., Helfter, C., Marchesini, L. B., Bosveld, F. C., van den
1057 Bulk, W. C. M., Elbers, J. A., Haapanala, S., Holst, J., Laurila, T., Lindroth, A.,
1058 Nemitz, E., Röckmann, T., Vermeulen, A. T., and Mammarella, I.: Evaluating the
1059 performance of commonly used gas analysers for methane eddy covariance flux
1060 measurements: the InGOS inter-comparison field experiment, *Biogeosciences*, 11,
1061 3163-3186, 2014.

1062 Peltola, O., Hensen, A., Marchesini, L. B., Helfter, C., Bosveld, F. C., van den
1063 Bulk, W. C. M., Haapanala, S., van Huissteden, J., Laurila, T., Lindroth, A., Nemitz,
1064 E., Röckmann, T., Vermeulen, A. T., and Mammarella, I.: Studying the spatial
1065 variability of methane flux with five eddy covariance towers of varying height,
1066 *Agricultural and Forest Meteorology*, 214, 456-472, 2015.

1067 Quay, P., Stutsman, J., Wilbur, D., Snover, A., Dlugokenky, E., and Brown, T.:
1068 The isotopic composition of atmospheric methane, *Global Biogeochem Cy*, 13, 445-
1069 461, 1999.

1070 Rasmussen, R. A. and Khalil, M. A. K.: Atmospheric Methane (CH₄) - Trends
1071 and Seasonal Cycles, *J. Geophys. Res.*, 86, 9826-9832, 1981.

1072 Rigby, M., Manning, A. J., and Prinn, R. G.: The value of high-frequency, high-
1073 precision methane isotopologue measurements for source and sink estimation, *J.*
1074 *Geophys. Res.*, 117, 2012.

1075 Röckmann, T., Brass, M., Borchers, R., and Engel, A.: The isotopic composition
1076 of methane in the stratosphere: High-altitude balloon sample measurements, *Atm.*
1077 *Chem. Phys.*, 11, 13287-13304, 2011.

1078 Sanderson, M. G.: Biomass of termites and their emissions of methane and
1079 carbon dioxide: A global database, *Global Biogeochem. Cycles*, 10, 543-557, 1996.

1080 Sapart, C. J., Monteil, G., Prokopiou, M., van de Wal, R. S. W., Kaplan, J. O.,
1081 Sperlich, P., Krumhardt, K. M., van der Veen, C., Houweling, S., Krol, M. C.,
1082 Blunier, T., Sowers, T., Martinerie, P., Witrant, E., Dahl-Jensen, D., and Röckmann,
1083 T.: Natural and anthropogenic variations in methane sources during the past two
1084 millennia, *Nature*, 490, 85-88, 2012.

1085 Sapart, C. J., Veen, C. v. d., Vigano, I., Brass, M., Wal, R. S. W. v. d., Bock, M.,
1086 Fischer, H., Sowers, T., Buizert, C., Sperlich, P., Blunier, T., Behrens, M., Schmitt, J.,

1087 Seth, B., and Röckmann, T.: Simultaneous stable isotope analysis of methane and
1088 nitrous oxide on ice core samples, *Atmos. Meas. Tech.*, 4, 2607-2618, 2011.

1089 Saueressig, G., Bergamaschi, P., Crowley, J. N., Fischer, H., and Harris, G. W.:
1090 D/H kinetic isotope effect in the reaction $\text{CH}_4 + \text{Cl}$, *Geophys. Res. Lett.*, 23, 3619-
1091 3622, 1996.

1092 Saueressig, G., Crowley, J. N., Bergamaschi, P., Brühl, C., Brenninkmeijer, C. A.
1093 M., and Fischer, H.: Carbon 13 and D kinetic isotope effects in the reactions of CH_4
1094 with $\text{O}(^1\text{D})$ and OH : New laboratory measurements and their implications for the
1095 isotopic composition of stratospheric methane, *J. Geophys. Res.*, 106, 23127-23138,
1096 2001.

1097 Schmitt, J., Seth, B., Bock, M., van der Veen, C., Möller, L., Sapart, C. J.,
1098 Prokopiou, M., Sowers, T., Röckmann, T., and Fischer, H.: On the interference of Kr
1099 during carbon isotope analysis of methane using continuous-flow combustion-isotope
1100 ratio mass spectrometry, *Atmos. Meas. Tech.*, 6, 1425-1445, 2013.

1101 Seibert, P. and Frank, A.: Source-receptor matrix calculation with a Lagrangian
1102 particle dispersion model in backward mode, *Atmos. Chem. Phys.*, 4, 51-63, 2004.

1103 Snover, A. K. and Quay, P. D.: Hydrogen and carbon kinetic isotope effects
1104 during soil uptake of atmospheric methane, *Global Biogeochem. Cycles*, 14, 25-39,
1105 2000.

1106 Spahni, R., Chappellaz, J., Stocker, T. F., Louergue, L., Hausammann, G.,
1107 Kawamura, K., Flückiger, J., Schwander, J., Raynaud, D., Masson-Delmotte, V., and
1108 Jouzel, J.: Atmospheric Methane and Nitrous Oxide of the Late Pleistocene from
1109 Antarctic Ice Cores, *Science*, 310, 1317-1321, DOI: 1310.1126/science.1120132,
1110 2005.

1111 Spahni, R., Wania, R., Neef, L., Weele, M. v., Pison, I., Bousquet, P.,
1112 Frankenberg, C., Foster, P. N., Joos, F., Prentice, I. C., and Velthoven, P. v.:
1113 Constraining global methane emissions and uptake by ecosystems, *Biogeosciences*, 8,
1114 1643–1665, doi:1610.5194/bg-1648-1643-2011., 2011.

1115 Sperlich, P., Buizert, C., Jenk, T. M., Sapart, C. J., Prokopiou, M., Rockmann, T.,
1116 and Blunier, T.: An automated GC-C-GC-IRMS setup to measure palaeoatmospheric
1117 $\delta^{13}\text{C}\text{-CH}_4$, $\delta^{15}\text{N}\text{-N}_2\text{O}$ and $\delta^{18}\text{O}\text{-N}_2\text{O}$ in one ice core sample, *Atmos Meas Tech*, 6,
1118 2027-2041, 2013.

1119 Sperlich, P., Uitslag, N. A. M., Richter, J. M., Rothe, M., Geilmann, H., Veen, C.
1120 v., Röckmann, T., Blunier, T., and Brand, W. A.: Development and evaluation of a
1121 suite of isotope reference gases for methane in air, submitted to *Atmos. Meas. Tech.*
1122 *Disc.*, 2016. 2016.

1123 Stohl, A., Forster, C., Frank, A., Seibert, P., and Wotawa, G.: Technical note: The
1124 Lagrangian particle dispersion model FLEXPART version 6.2, *Atmos. Chem. Phys.*,
1125 5, 2461-2474, 2005.

1126 Sturm, P., Tuzson, B., Henne, S., and Emmenegger, L.: Tracking isotopic
1127 signatures of CO_2 at the high altitude site Jungfrauoch with laser spectroscopy:
1128 analytical improvements and representative results, *Atmos. Meas. Tech.*, 6, 1659-
1129 1671, 2013.

1130 Tarasova, O. A., Brenninkmeijer, C. A. M., Assonov, S. S., Elansky, N. F.,
1131 Röckmann, T., and Brass, M.: Atmospheric CH_4 along the Trans-Siberian railroad
1132 (TROICA) and river Ob: Source identification using stable isotope analysis, *Atmos.*
1133 *Environ.*, 40, 5617-5628, 2006.

1134 Tuzson, B., Henne, S., Brunner, D., Steinbacher, M., Mohn, J., Buchmann, B.,
1135 and Emmenegger, L.: Continuous isotopic composition measurements of tropospheric
1136 CO₂ at Jungfraujoch (3580 m a.s.l.), Switzerland: real-time observation of regional
1137 pollution events, *Atmos. Chem. Phys.*, 11, 1685-1696, 2011.

1138 Tuzson, B., Mohn, J., Zeeman, M. J., Werner, R. A., Eugster, W., Zahniser, M.
1139 S., Nelson, D. D., McManus, J. B., and Emmenegger, L.: High precision and
1140 continuous field measurements of $\delta^{13}\text{C}$ and $\delta^{18}\text{O}$ in carbon dioxide with a cryogen-
1141 free QCLAS, *Appl. Phys. B-Lasers and Optics*, 92, 451-458, 2008.

1142 Umezawa, T., Aoki, S., Nakazawa, T., and Morimoto, S.: A High-precision
1143 Measurement System for Carbon and Hydrogen Isotopic Ratios of Atmospheric
1144 Methane and Its Application to Air Samples Collected in the Western Pacific Region,
1145 *Journal of the Meteorological Society of Japan*, 87, 365-379, 2009.

1146 Umezawa, T., Machida, T., Aoki, S., and Nakazawa, T.: Contributions of natural
1147 and anthropogenic sources to atmospheric methane variations over western Siberia
1148 estimated from its carbon and hydrogen isotopes, *Global Biogeochem. Cycles*, 26,
1149 2012a.

1150 Umezawa, T., Machida, T., Ishijima, K., Matsueda, H., Sawa, Y., Patra, P. K.,
1151 Aoki, S., and Nakazawa, T.: Carbon and hydrogen isotopic ratios of atmospheric
1152 methane in the upper troposphere over the Western Pacific, *Atmos. Chem. Phys.*, 12,
1153 8095-8113, 2012b.

1154 Vermeulen, A. T., Hensen, A., Popa, M. E., van den Bulk, W. C. M., and
1155 Jongejan, P. A. C.: Greenhouse gas observations from Cabauw Tall Tower (1992-
1156 2010), *Atmos. Meas. Tech.*, 4, 617-644, 2011.

1157 Wächter, H., Mohn, J., Tuzson, B., Emmenegger, L., and Sigrist, M. W.:
1158 Determination of N₂O isotopomers with quantum cascade laser based absorption
1159 spectroscopy, *Optics Express*, 16, 9239-9244, 2008.

1160 WMO: 17th WMO/IAEA Meeting on Carbon Dioxide, Other Greenhouse Gases,
1161 and Related Measurement Techniques (GGMT-2013) 10-13 June 2013, GAW Report
1162 No. 213,, World Meteorological Organization, Geneva, Switzerland, Beijing, China,
1163 2014.

1164 Wolf, B., Merbold, L., Decock, C., Tuzson, B., Harris, E., Six, J., Emmenegger,
1165 L., and Mohn, J.: First on-line isotopic characterization of N₂O above intensively
1166 managed grassland, *Biogeosciences*, 12, 2517-2531, 2015.

1167 Yamada, K., Ozaki, Y., Nakagawa, F., Tanaka, M., and Yoshida, N.: An
1168 improved method for measurement of the hydrogen isotope ratio of atmospheric
1169 methane and its application to a Japanese urban atmosphere, *Atmos. Environ.*, 37,
1170 1975-1982, 2003.

1171 Zazzeri, G., Lowry, D., Fisher, R. E., France, J. L., Lanoiselle, M., and Nisbet, E.
1172 G.: Plume mapping and isotopic characterisation of anthropogenic methane sources,
1173 *Atmos. Environ.*, 110, 151-162, 2015.

1174